

Lectures on Gravitational Lensing

Ramesh NARAYAN

Harvard-Smithsonian Center for Astrophysics

60 Garden Street

Cambridge, MA 02138, USA

Matthias BARTELMANN

Max-Planck-Institut für Astrophysik

P.O. Box 1523, D-85740 Garching, Germany

October 6, 2018

Contents

1	Introduction	2
2	Lensing by Point Masses in the Universe	5
2.1	Basics of Gravitational Lensing	5
2.1.1	Effective Refractive Index of a Gravitational Field	6
2.1.2	Thin Screen Approximation	8
2.1.3	Lensing Geometry and Lens Equation	10
2.1.4	Einstein Radius	11
2.1.5	Imaging by a Point Mass Lens	12
2.2	Microlensing in the Galaxy	14
2.2.1	Basic Relations	14
2.2.2	Ongoing Galactic Microlensing Searches	16
2.2.3	Early Results on Optical Depths	16
2.2.4	Other Interesting Discoveries	18
2.3	Extragalactic Microlenses	19
2.3.1	Point Masses in the Universe	19
2.3.2	Current Upper Limits on Ω_M in Point Masses	20
2.3.3	Microlensing in QSO 2237+0305	20
3	Lensing by Galaxies	21
3.1	Lensing by a Singular Isothermal Sphere	22
3.2	Effective Lensing Potential	23
3.3	Gravitational Lensing via Fermat's Principle	24
3.3.1	The Time-Delay Function	24
3.3.2	Properties of the Time-Delay Function	27
3.4	Circularly Symmetric Lens Models	29
3.5	Non-Circularly-Symmetric Lens Models	31
3.5.1	Elliptical Galaxy Model	31
3.5.2	External Shear	32
3.5.3	Image Configurations with a Non-Circularly Symmetric Lens	32
3.6	Studies of Galaxy Lensing	33
3.6.1	Detailed Models of Individual Cases of Lensing	33
3.6.2	Statistical Modeling of Lens Populations	36

3.7	Astrophysical Results from Galaxy Lensing	36
3.7.1	Galaxy Structure	36
3.7.2	Galaxy Formation and Evolution	37
3.7.3	Constraint on CDM	37
3.7.4	Hubble Constant	38
3.7.5	Cosmological Constant	40
4	Lensing by Galaxy Clusters and Large-Scale Structure	40
4.1	Strong Lensing by Clusters — Giant Arcs	40
4.1.1	Basic Optics	41
4.1.2	Cluster Mass Inside a Giant Arc	41
4.1.3	Asphericity of Cluster Mass	43
4.1.4	Core Radii	43
4.1.5	Radial Density Profile	44
4.1.6	Mass Sub-Condensations	45
4.1.7	Lensing Results vs. Other Mass Determinations	45
4.2	Weak Lensing by Clusters — Arclets	47
4.2.1	The Kaiser & Squires Algorithm	47
4.2.2	Practical Details and Subtleties	48
4.2.3	Eliminating the Mass Sheet Degeneracy by Measuring the Convergence	50
4.2.4	Determining Source Redshifts	51
4.2.5	Finite Field Methods	51
4.2.6	Results from Weak Lensing	51
4.3	Weak Lensing by Large-Scale Structure	52
4.3.1	Magnification and Shear in ‘Empty’ Fields	52
4.3.2	Large-Scale QSO-Galaxy Correlations	53
4.3.3	Outlook: Detecting Dark Matter Concentrations	53

1 Introduction

One of the consequences of Einstein’s General Theory of Relativity is that light rays are deflected by gravity. Although this discovery was made only in this century, the possibility that there could be such a deflection had been suspected much earlier, by Newton and Laplace among others. Soldner (1804) calculated the magnitude of the deflection due to the Sun, assuming that light consists of material particles and using Newtonian gravity. Later, Einstein (1911) employed the equivalence principle to calculate the deflection angle and re-derived Soldner’s formula. Later yet, Einstein (1915) applied the full field equations of General Relativity and discovered that the deflection angle is actually twice his previous result, the factor of two arising because of the curvature of the metric. According to this formula, a light ray which tangentially grazes the surface of the Sun is deflected by $1.7''$. Einstein’s final result was confirmed in 1919 when the apparent angular shift of stars close to the limb of the Sun (see Fig. 1) was measured during a total solar eclipse (Dyson, Eddington, & Davidson 1920). The quantitative agreement between the measured shift and Einstein’s prediction was immediately perceived as compelling evidence in support of the theory of General Relativity. The deflection of light by massive bodies, and the phenomena resulting therefrom, are now referred to as *Gravitational Lensing*.

Eddington (1920) noted that under certain conditions there may be multiple light paths connecting a source and an observer. This implies that gravitational lensing can give rise to multiple images of a single source. Chwolson (1924) considered the creation of fictitious double stars by gravitational lensing of stars by stars, but did not comment on whether the phenomenon could actually be observed. Einstein (1936) discussed the same problem and concluded that there is little chance of observing lensing phenomena caused by stellar-mass lenses. His reason was that the angular image splitting caused by a stellar-mass lens is too small to be resolved by an optical telescope.

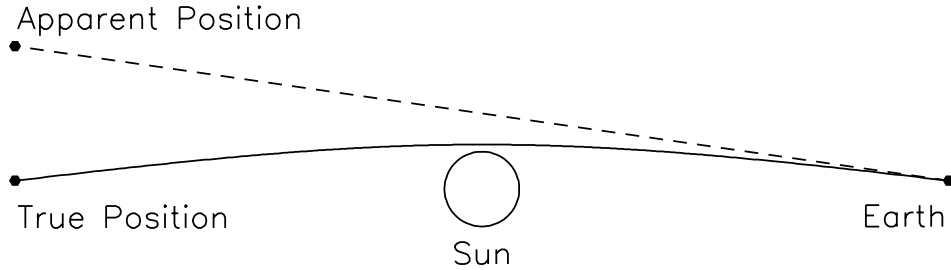


Figure 1: Angular deflection of a ray of light passing close to the limb of the Sun. Since the light ray is bent toward the Sun, the apparent positions of stars move away from the Sun.

Zwicky (1937a) elevated gravitational lensing from a curiosity to a field with great potential when he pointed out that galaxies can split images of background sources by a large enough angle to be observed. At that time, galaxies were commonly believed to have masses of $\sim 10^9 M_\odot$. However, Zwicky had applied the virial theorem to the Virgo and Coma clusters of galaxies and had derived galaxy masses of $\sim 4 \times 10^{11} M_\odot$. Zwicky argued that the deflection of light by galaxies would not only furnish an additional test of General Relativity, but would also magnify distant galaxies which would otherwise remain undetected, and would allow accurate determination of galaxy masses. Zwicky (1937b) even calculated the probability of lensing by galaxies and concluded that it is on the order of one per cent for a source at reasonably large redshift.

Virtually all of Zwicky's predictions have come true. Lensing by galaxies is a major sub-discipline of gravitational lensing today. The most accurate mass determinations of the central regions of galaxies are due to gravitational lensing, and the cosmic telescope effect of gravitational lenses has enabled us to study faint and distant galaxies which happen to be strongly magnified by galaxy clusters. The statistics of gravitational lensing events, whose order of magnitude Zwicky correctly estimated, offers one of the promising ways of inferring cosmological parameters.

In a stimulating paper, Refsdal (1964) described how the Hubble constant H_0 could in principle be measured through gravitational lensing of a variable source. Since the light travel times for the various images are unequal, intrinsic variations of the source would be observed at different times in the images. The time delay between images is proportional to the difference in the absolute lengths of the light paths, which in turn is proportional to H_0^{-1} . Thus, if the time delay is measured and if an accurate model of a lensed source is developed, the Hubble constant could be measured.

All of these ideas on gravitational lensing remained mere speculation until real examples of gravitational lensing were finally discovered. The stage for this was set by the discovery of quasars (Schmidt 1963) which revealed a class of sources that is ideal for studying the effects of gravitational lensing. Quasars are distant, and so the probability that they are lensed by intervening galaxies is sufficiently large. Yet, they are bright enough to be detected even at cosmological distances. Moreover, their optical emission region is very compact, much smaller than the typical scales of galaxy lenses. The resulting magnifications can therefore be very large, and multiple image components are well separated and easily detected.

Walsh, Carswell, & Weymann (1979) discovered the first example of gravitational lensing, the quasar QSO 0957+561A,B. This source consists of two images, A and B, separated by $6''$. Evidence that 0957+561A,B does indeed correspond to twin lensed images of a single QSO is provided by (i) the similarity of the spectra of the two images, (ii) the fact that the flux ratio between the images is the same in the optical and radio wavebands, (iii) the presence of a foreground galaxy between the images, and (iv) VLBI observations which show detailed correspondence between various knots of

emission in the two radio images. Over a dozen convincing examples of multiple-imaged quasars are known today (Keeton & Kochanek 1996) and the list continues to grow.

Paczynski (1986b) revived the idea of lensing of stars by stars when he showed that at any given time one out of a million stars in the Large Magellanic Cloud (LMC) might be measurably magnified by the gravitational lens effect of an intervening star in the halo of our Galaxy. The magnification events, which are called *microlensing* events, have time scales between two hours and two years for lens masses between $10^{-6} M_{\odot}$ and $10^2 M_{\odot}$. Initially, it was believed that the proposed experiment of monitoring the light curves of a million stars would never be feasible, especially since the light curves have to be sampled frequently and need to be distinguished from light curves of intrinsically variable stars. Nevertheless, techniques have advanced so rapidly that today four separate collaborations have successfully detected microlensing events (Alcock et al. 1993; Aubourg et al. 1993; Udalski et al. 1993; Alard 1995), and this field has developed into an exciting method for studying the nature and distribution of mass in our Galaxy.

Einstein rings, a particularly interesting manifestation of gravitational lensing, were discovered first in the radio waveband by Hewitt et al. (1987). About half a dozen radio rings are now known and these sources permit the most detailed modeling yet of the mass distributions of lensing galaxies.

Gravitational lensing by galaxy clusters had been considered theoretically even before the discovery of QSO 0957+561. The subject entered the observational realm with the discovery of giant blue luminous *arcs* in the galaxy clusters A 370 and Cl 2244 (Soucail et al. 1987a,b; Lynds & Petrosian 1986). Paczynski (1987) proposed that the arcs are the images of background galaxies which are strongly distorted and elongated by the gravitational lens effect of the foreground cluster. This explanation was confirmed when the first arc redshifts were measured and found to be significantly greater than that of the clusters.

Apart from the spectacular giant luminous arcs, which require special alignment between the cluster and the background source, clusters also coherently distort the images of other faint background galaxies (Tyson 1988). These distortions are mostly weak, and the corresponding images are referred to as *arclets* (Fort et al. 1988; Tyson, Valdes, & Wenk 1990). Observations of arclets can be used to reconstruct parameter-free, two-dimensional mass maps of the lensing cluster (Kaiser & Squires 1993). This technique has attracted a great deal of interest, and two-dimensional maps have been obtained of several galaxy clusters (Bonnet et al. 1993; Bonnet, Mellier, & Fort 1994; Fahlman et al. 1994; Broadhurst 1995; Smail et al. 1995; Tyson & Fischer 1995; Squires et al. 1996; Seitz et al. 1996).

As this brief summary indicates, gravitational lensing manifests itself through a very broad and interesting range of phenomena. At the same time, lensing has developed into a powerful tool to study a host of important questions in astrophysics. The applications of gravitational lensing may be broadly classified under three categories:

- The magnification effect enables us to observe objects which are too distant or intrinsically too faint to be observed without lensing. Lenses therefore act as cosmic telescopes and allow us to infer source properties far below the resolution limit or sensitivity limit of current observations. However, since we do not have the ability to point the cosmic telescope at any particular object of interest but have to work with whatever nature gives us, the results have been only modestly interesting.
- Gravitational lensing depends solely on the projected, two-dimensional mass distribution of the lens, and is independent of the luminosity or composition of the lens. Lensing therefore offers an ideal way to detect and study dark matter, and to explore the growth and structure of mass condensations in the universe.
- Many properties of individual lens systems or samples of lensed objects depend on the age, the scale, and the overall geometry of the universe. The Hubble constant, the cosmological constant, and the density parameter of the universe can be significantly constrained through lensing.

The article is divided into three main sections. Sect. 2 discusses the effects of point-mass lenses, Sect. 3 considers galaxy-scale lenses, and Sect. 4 discusses lensing by galaxy clusters and large-scale structure in the universe. References to the original literature are given throughout the text. The following are some general or specialized review articles and monographs:

Monograph

- Schneider, P., Ehlers, J., & Falco, E.E. 1992, *Gravitational Lenses* (Berlin: Springer Verlag)

General Reviews

- Blandford, R.D., & Narayan, R. 1992, *Cosmological Applications of Gravitational Lensing*, Ann. Rev. Astr. Ap., 30, 311
- Refsdal, S., & Surdej, J. 1994, *Gravitational Lenses*, Rep. Progr. Phys., 57, 117
- Schneider, P. 1996, *Cosmological Applications of Gravitational Lensing*, Lecture Notes in Physics, eds. E. Martínez-González & J.L. Sanz, in press (Berlin: Springer Verlag)
- Wu, X.-P. 1996, *Gravitational Lensing in the Universe*, Fundamentals of Cosmic Physics, in press

Special Reviews

- Bartelmann, M., & Narayan, R. 1995, *Gravitational Lensing and the Mass Distribution of Clusters*, in: *Dark Matter*, AIP Conf. Proc. 336, eds. S.S. Holt & C.L. Bennett (New York: AIP Press)
- Fort, B., & Mellier, Y. 1994, *Arc(let)s in Clusters of Galaxies*, Astr. Ap. Rev., 5, 239
- Keeton II, C.R. & Kochanek, C.S. 1996, *Summary of Data on Secure Multiply-Imaged Systems*, in: *Cosmological Applications of Gravitational Lensing*, IAU Symp. 173, eds. C.S. Kochanek & J.N. Hewitt
- Paczyński, B. 1996, *Gravitational Microlensing in the Local Group*, Ann. Rev. Astr. Ap., in press
- Roulet, E., & Mollerach, S. 1996, *Microlensing*, Physics Reports, in press

2 Lensing by Point Masses in the Universe

2.1 Basics of Gravitational Lensing

The propagation of light in arbitrary curved spacetimes is in general a complicated theoretical problem. However, for almost all cases of relevance to gravitational lensing, we can assume that the overall geometry of the universe is well described by the Friedmann-Lemaître-Robertson-Walker metric and that the matter inhomogeneities which cause the lensing are no more than local perturbations. Light paths propagating from the source past the lens to the observer can then be broken up into three distinct zones. In the first zone, light travels from the source to a point close to the lens through unperturbed spacetime. In the second zone, near the lens, light is deflected. Finally, in the third zone, light again travels through unperturbed spacetime. To study light deflection close to the lens, we can assume a locally flat, Minkowskian spacetime which is weakly perturbed by the Newtonian gravitational potential of the mass distribution constituting the lens. This approach is legitimate if the Newtonian potential Φ is small, $|\Phi| \ll c^2$, and if the peculiar velocity v of the lens is small, $v \ll c$.

These conditions are satisfied in virtually all cases of astrophysical interest. Consider for instance a galaxy cluster at redshift ~ 0.3 which deflects light from a source at redshift ~ 1 . The

distances from the source to the lens and from the lens to the observer are ~ 1 Gpc, or about three orders of magnitude larger than the diameter of the cluster. Thus zone 2 is limited to a small local segment of the total light path. The relative peculiar velocities in a galaxy cluster are $\sim 10^3 \text{ km s}^{-1} \ll c$, and the Newtonian potential is $|\Phi| < 10^{-4} c^2 \ll c^2$, in agreement with the conditions stated above.

2.1.1 Effective Refractive Index of a Gravitational Field

In view of the simplifications just discussed, we can describe light propagation close to gravitational lenses in a locally Minkowskian spacetime perturbed by the gravitational potential of the lens to first post-Newtonian order. The effect of spacetime curvature on the light paths can then be expressed in terms of an effective index of refraction n , which is given by (e.g. Schneider et al. 1992)

$$n = 1 - \frac{2}{c^2} \Phi = 1 + \frac{2}{c^2} |\Phi|. \quad (1)$$

Note that the Newtonian potential is negative if it is defined such that it approaches zero at infinity. As in normal geometrical optics, a refractive index $n > 1$ implies that light travels slower than in free vacuum. Thus, the effective speed of a ray of light in a gravitational field is

$$v = \frac{c}{n} \simeq c - \frac{2}{c} |\Phi|. \quad (2)$$

Figure 2 shows the deflection of light by a glass prism. The speed of light is reduced inside the prism. This reduction of speed causes a delay in the arrival time of a signal through the prism relative to another signal traveling at speed c . In addition, it causes wavefronts to tilt as light propagates from one medium to another, leading to a bending of the light ray around the thick end of the prism.

The same effects are seen in gravitational lensing. Because the effective speed of light is reduced in a gravitational field, light rays are delayed relative to propagation in vacuum. The total time delay Δt is obtained by integrating over the light path from the observer to the source:

$$\Delta t = \int_{\text{source}}^{\text{observer}} \frac{2}{c^3} |\Phi| dl. \quad (3)$$

This is called the Shapiro delay (Shapiro 1964).

As in the case of the prism, light rays are deflected when they pass through a gravitational field. The deflection is the integral along the light path of the gradient of n perpendicular to the light path, i.e.

$$\vec{\alpha} = - \int \vec{\nabla}_{\perp} n dl = \frac{2}{c^2} \int \vec{\nabla}_{\perp} \Phi dl. \quad (4)$$

In all cases of interest the deflection angle is very small. We can therefore simplify the computation of the deflection angle considerably if we integrate $\vec{\nabla}_{\perp} n$ not along the deflected ray, but along an unperturbed light ray with the same impact parameter. (As an aside we note that while the procedure is straightforward with a single lens, some care is needed in the case of multiple lenses at different distances from the source. With multiple lenses, one takes the unperturbed ray from the source as the reference trajectory for calculating the deflection by the first lens, the deflected ray from the first lens as the reference unperturbed ray for calculating the deflection by the second lens, and so on.)

As an example, we now evaluate the deflection angle of a point mass M (cf. Fig. 3). The Newtonian potential of the lens is

$$\Phi(b, z) = - \frac{GM}{(b^2 + z^2)^{1/2}}, \quad (5)$$

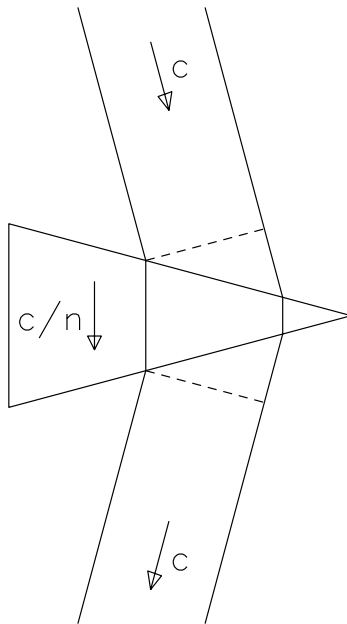


Figure 2: Light deflection by a prism. The refractive index $n > 1$ of the glass in the prism reduces the effective speed of light to c/n . This causes light rays to be bent around the thick end of the prism, as indicated. The dashed lines are wavefronts. Although the geometrical distance between the wavefronts along the two rays is different, the travel time is the same because the ray on the left travels through a larger thickness of glass.

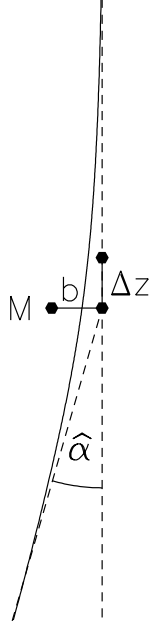


Figure 3: Light deflection by a point mass. The unperturbed ray passes the mass at impact parameter b and is deflected by the angle $\hat{\alpha}$. Most of the deflection occurs within $\Delta z \sim \pm b$ of the point of closest approach.

where b is the impact parameter of the unperturbed light ray, and z indicates distance along the unperturbed light ray from the point of closest approach. We therefore have

$$\vec{\nabla}_{\perp} \Phi(b, z) = \frac{GM \vec{b}}{(b^2 + z^2)^{3/2}}, \quad (6)$$

where \vec{b} is orthogonal to the unperturbed ray and points toward the point mass. Equation (6) then yields the deflection angle

$$\hat{\alpha} = \frac{2}{c^2} \int \vec{\nabla}_{\perp} \Phi dz = \frac{4GM}{c^2 b}. \quad (7)$$

Note that the Schwarzschild radius of a point mass is

$$R_S = \frac{2GM}{c^2}, \quad (8)$$

so that the deflection angle is simply twice the inverse of the impact parameter in units of the Schwarzschild radius. As an example, the Schwarzschild radius of the Sun is 2.95 km, and the solar radius is 6.96×10^5 km. A light ray grazing the limb of the Sun is therefore deflected by an angle $(5.9/7.0) \times 10^{-5}$ radians = $1.7''$.

2.1.2 Thin Screen Approximation

Figure 3 illustrates that most of the light deflection occurs within $\Delta z \sim \pm b$ of the point of closest encounter between the light ray and the point mass. This Δz is typically much smaller than the distances between observer and lens and between lens and source. The lens can therefore be

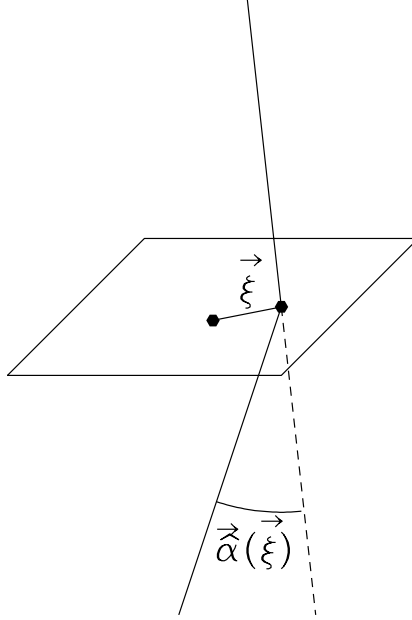


Figure 4: A light ray which intersects the lens plane at $\vec{\xi}$ is deflected by an angle $\vec{\alpha}(\vec{\xi})$.

considered thin compared to the total extent of the light path. The mass distribution of the lens can then be projected along the line-of-sight and be replaced by a mass sheet orthogonal to the line-of-sight. The plane of the mass sheet is commonly called the lens plane. The mass sheet is characterized by its surface mass density

$$\Sigma(\vec{\xi}) = \int \rho(\vec{\xi}, z) dz , \quad (9)$$

where $\vec{\xi}$ is a two-dimensional vector in the lens plane. The deflection angle at position $\vec{\xi}$ is the sum of the deflections due to all the mass elements in the plane:

$$\vec{\alpha}(\vec{\xi}) = \frac{4G}{c^2} \int \frac{(\vec{\xi} - \vec{\xi}') \Sigma(\vec{\xi}')}{|\vec{\xi} - \vec{\xi}'|^2} d^2 \xi' . \quad (10)$$

Figure 4 illustrates the situation.

In general, the deflection angle is a two-component vector. In the special case of a circularly symmetric lens, we can shift the coordinate origin to the center of symmetry and reduce light deflection to a one-dimensional problem. The deflection angle then points toward the center of symmetry, and its modulus is

$$\hat{\alpha}(\xi) = \frac{4GM(\xi)}{c^2 \xi} , \quad (11)$$

where ξ is the distance from the lens center and $M(\xi)$ is the mass enclosed within radius ξ ,

$$M(\xi) = 2\pi \int_0^\xi \Sigma(\xi') \xi' d\xi' . \quad (12)$$

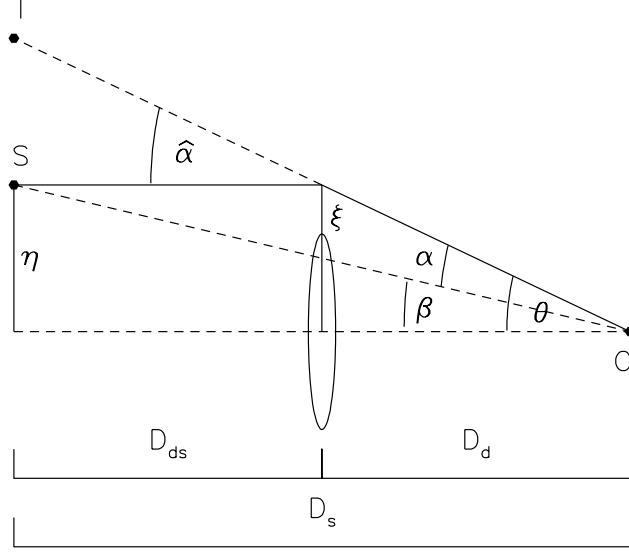


Figure 5: Illustration of a gravitational lens system. The light ray propagates from the source S at transverse distance η from the optic axis to the observer O , passing the lens at transverse distance ξ . It is deflected by an angle $\hat{\alpha}$. The angular separations of the source and the image from the optic axis as seen by the observer are β and θ , respectively. The reduced deflection angle α and the actual deflection angle $\hat{\alpha}$ are related by eq. (13). The distances between the observer and the source, the observer and the lens, and the lens and the source are D_s , D_d , and D_{ds} , respectively.

2.1.3 Lensing Geometry and Lens Equation

The geometry of a typical gravitational lens system is shown in Fig. 5. A light ray from a source S is deflected by the angle $\vec{\alpha}$ at the lens and reaches an observer O . The angle between the (arbitrarily chosen) optic axis and the true source position is $\vec{\beta}$, and the angle between the optic axis and the image I is $\vec{\theta}$. The (angular diameter) distances between observer and lens, lens and source, and observer and source are D_d , D_{ds} , and D_s , respectively.

It is now convenient to introduce the reduced deflection angle

$$\vec{\alpha} = \frac{D_{ds}}{D_s} \vec{\hat{\alpha}}. \quad (13)$$

From Fig. 5 we see that $\theta D_s = \beta D_s - \hat{\alpha} D_{ds}$. Therefore, the positions of the source and the image are related through the simple equation

$$\vec{\beta} = \vec{\theta} - \vec{\alpha}(\vec{\theta}). \quad (14)$$

Equation (14) is called the *lens equation*, or ray-tracing equation. It is nonlinear in the general case, and so it is possible to have multiple images $\vec{\theta}$ corresponding to a single source position $\vec{\beta}$. As Fig. 5 shows, the lens equation is trivial to derive and requires merely that the following Euclidean relation should exist between the angle enclosed by two lines and their separation,

$$\text{separation} = \text{angle} \times \text{distance}. \quad (15)$$

It is not obvious that the same relation should also hold in curved spacetimes. However, if the distances $D_{d,s,ds}$ are *defined* such that eq. (15) holds, then the lens equation must obviously be true. Distances so defined are called angular-diameter distances, and eqs. (13), (14) are valid only when these distances are used. Note that in general $D_{ds} \neq D_s - D_d$.

As an instructive special case consider a lens with a constant surface-mass density. From eq. (11), the (reduced) deflection angle is

$$\alpha(\theta) = \frac{D_{ds}}{D_s} \frac{4G}{c^2 \xi} (\Sigma \pi \xi^2) = \frac{4\pi G \Sigma}{c^2} \frac{D_d D_{ds}}{D_s} \theta, \quad (16)$$

where we have set $\xi = D_d \theta$. In this case, the lens equation is linear; that is, $\beta \propto \theta$. Let us define a critical surface-mass density

$$\Sigma_{cr} = \frac{c^2}{4\pi G} \frac{D_s}{D_d D_{ds}} = 0.35 \text{ g cm}^{-2} \left(\frac{D}{1 \text{ Gpc}} \right)^{-1}, \quad (17)$$

where the effective distance D is defined as the combination of distances

$$D = \frac{D_d D_{ds}}{D_s}. \quad (18)$$

For a lens with a constant surface mass density Σ_{cr} , the deflection angle is $\alpha(\theta) = \theta$, and so $\beta = 0$ for all θ . Such a lens focuses perfectly, with a well-defined focal length. A typical gravitational lens, however, behaves quite differently. Light rays which pass the lens at different impact parameters cross the optic axis at different distances behind the lens. Considered as an optical device, a gravitational lens therefore has almost all aberrations one can think of. However, it does not have any chromatic aberration because the geometry of light paths is independent of wavelength.

A lens which has $\Sigma > \Sigma_{cr}$ somewhere within it is referred to as being *supercritical*. Usually, multiple imaging occurs only if the lens is supercritical, but there are exceptions to this rule (e.g., Subramanian & Cowling 1986).

2.1.4 Einstein Radius

Consider now a circularly symmetric lens with an arbitrary mass profile. According to eqs. (11) and (13), the lens equation reads

$$\beta(\theta) = \theta - \frac{D_{ds}}{D_d D_s} \frac{4GM(\theta)}{c^2 \theta}. \quad (19)$$

Due to the rotational symmetry of the lens system, a source which lies exactly on the optic axis ($\beta = 0$) is imaged as a ring if the lens is supercritical. Setting $\beta = 0$ in eq. (19) we obtain the radius of the ring to be

$$\theta_E = \left[\frac{4GM(\theta_E)}{c^2} \frac{D_{ds}}{D_d D_s} \right]^{1/2}. \quad (20)$$

This is referred to as the *Einstein radius*. Figure 6 illustrates the situation. Note that the Einstein radius is not just a property of the lens, but depends also on the various distances in the problem.

The Einstein radius provides a natural angular scale to describe the lensing geometry for several reasons. In the case of multiple imaging, the typical angular separation of images is of order $2\theta_E$. Further, sources which are closer than about θ_E to the optic axis experience strong lensing in the sense that they are significantly magnified, whereas sources which are located well outside the Einstein ring are magnified very little. In many lens models, the Einstein ring also represents roughly the boundary between source positions that are multiply-imaged and those that are only singly-imaged. Finally, by comparing eqs. (17) and (20) we see that the mean surface mass density inside the Einstein radius is just the critical density Σ_{cr} .

For a point mass M , the Einstein radius is given by

$$\theta_E = \left(\frac{4GM}{c^2} \frac{D_{ds}}{D_d D_s} \right)^{1/2}. \quad (21)$$

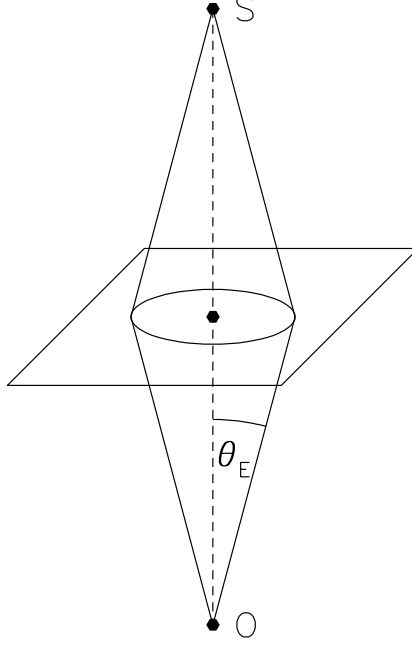


Figure 6: A source S on the optic axis of a circularly symmetric lens is imaged as a ring with an angular radius given by the Einstein radius θ_E .

To give two illustrative examples, we consider lensing by a star in the Galaxy, for which $M \sim M_\odot$ and $D \sim 10$ kpc, and lensing by a galaxy at a cosmological distance with $M \sim 10^{11} M_\odot$ and $D \sim 1$ Gpc. The corresponding Einstein radii are

$$\begin{aligned}\theta_E &= (0.9 \text{ mas}) \left(\frac{M}{M_\odot} \right)^{1/2} \left(\frac{D}{10 \text{ kpc}} \right)^{-1/2}, \\ \theta_E &= (0.9'') \left(\frac{M}{10^{12} M_\odot} \right)^{1/2} \left(\frac{D}{\text{Gpc}} \right)^{-1/2}.\end{aligned}\tag{22}$$

2.1.5 Imaging by a Point Mass Lens

For a point mass lens, we can use the Einstein radius (20) to rewrite the lens equation in the form

$$\beta = \theta - \frac{\theta_E^2}{\theta}.\tag{23}$$

This equation has two solutions,

$$\theta_\pm = \frac{1}{2} \left(\beta \pm \sqrt{\beta^2 + 4\theta_E^2} \right).\tag{24}$$

Any source is imaged twice by a point mass lens. The two images are on either side of the source, with one image inside the Einstein ring and the other outside. As the source moves away from the lens (i.e. as β increases), one of the images approaches the lens and becomes very faint, while the other image approaches closer and closer to the true position of the source and tends toward a magnification of unity.

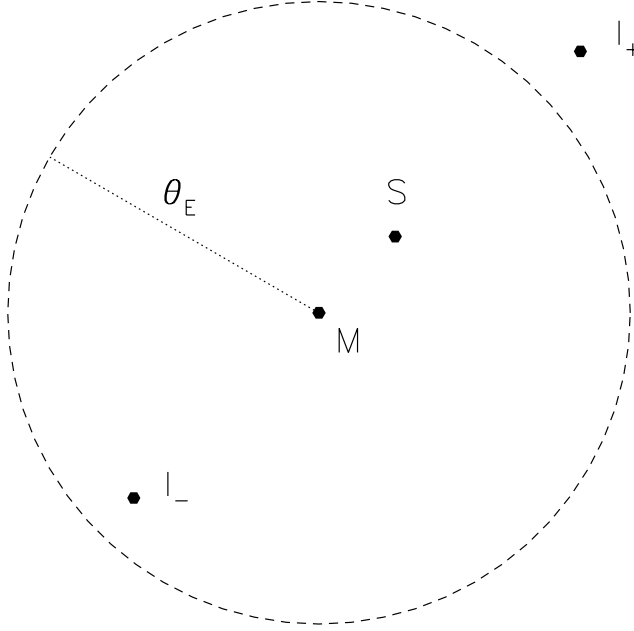


Figure 7: Relative locations of the source S and images I_+ , I_- lensed by a point mass M. The dashed circle is the Einstein ring with radius θ_E . One image is inside the Einstein ring and the other outside.

Gravitational light deflection preserves surface brightness (because of Liouville's theorem), but gravitational lensing changes the apparent solid angle of a source. The total flux received from a gravitationally lensed image of a source is therefore changed in proportion to the ratio between the solid angles of the image and the source,

$$\text{magnification} = \frac{\text{image area}}{\text{source area}} . \quad (25)$$

Figure 8 shows the magnified images of a source lensed by a point mass.

For a circularly symmetric lens, the magnification factor μ is given by

$$\mu = \frac{\theta}{\beta} \frac{d\theta}{d\beta} . \quad (26)$$

For a point mass lens, which is a special case of a circularly symmetric lens, we can substitute for β using the lens equation (23) to obtain the magnifications of the two images,

$$\mu_{\pm} = \left[1 - \left(\frac{\theta_E}{\theta_{\pm}} \right)^4 \right]^{-1} = \frac{u^2 + 2}{2u\sqrt{u^2 + 4}} \pm \frac{1}{2} , \quad (27)$$

where u is the angular separation of the source from the point mass in units of the Einstein angle, $u = \beta\theta_E^{-1}$. Since $\theta_- < \theta_E$, $\mu_- < 0$, and hence the magnification of the image which is inside the Einstein ring is negative. This means that this image has its parity flipped with respect to the source. The net magnification of flux in the two images is obtained by adding the absolute magnifications,

$$\mu = |\mu_+| + |\mu_-| = \frac{u^2 + 2}{u\sqrt{u^2 + 4}} . \quad (28)$$

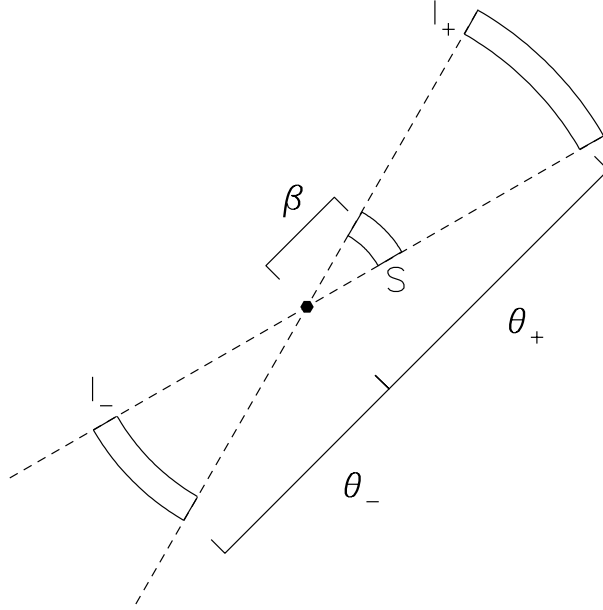


Figure 8: Magnified images of a source lensed by a point mass.

When the source lies on the Einstein radius, we have $\beta = \theta_E$, $u = 1$, and the total magnification becomes

$$\mu = 1.17 + 0.17 = 1.34 . \quad (29)$$

How can lensing by a point mass be detected? Unless the lens is massive ($M > 10^6 M_\odot$ for a cosmologically distant source), the angular separation of the two images is too small to be resolved. However, even when it is not possible to see the multiple images, the magnification can still be detected if the lens and source move relative to each other, giving rise to lensing-induced time variability of the source (Chang & Refsdal 1979; Gott 1981). When this kind of variability is induced by stellar mass lenses it is referred to as *microlensing*. Microlensing was first observed in the multiply-imaged QSO 2237+0305 (Irwin et al. 1989), and may also have been seen in QSO 0957+561 (Schild & Smith 1991; see also Sect. 3.7.4). Paczyński (1986b) had the brilliant idea of using microlensing to search for so-called *Massive Astrophysical Compact Halo Objects* (MACHOs, Griest 1991) in the Galaxy. We discuss this topic in some depth in Sect. 2.2.

2.2 Microlensing in the Galaxy

2.2.1 Basic Relations

If the closest approach between a point mass lens and a source is $\leq \theta_E$, the peak magnification in the lensing-induced light curve is $\mu_{\max} \geq 1.34$. A magnification of 1.34 corresponds to a brightening by 0.32 magnitudes, which is easily detectable. Paczyński (1986b) proposed monitoring millions of stars in the LMC to look for such magnifications in a small fraction of the sources. If enough events are detected, it should be possible to map the distribution of stellar-mass objects in our Galaxy.

Perhaps the biggest problem with Paczyński's proposal is that monitoring a million stars or more primarily leads to the detection of a huge number of variable stars. The intrinsically variable sources must somehow be distinguished from stars whose variability is caused by microlensing.

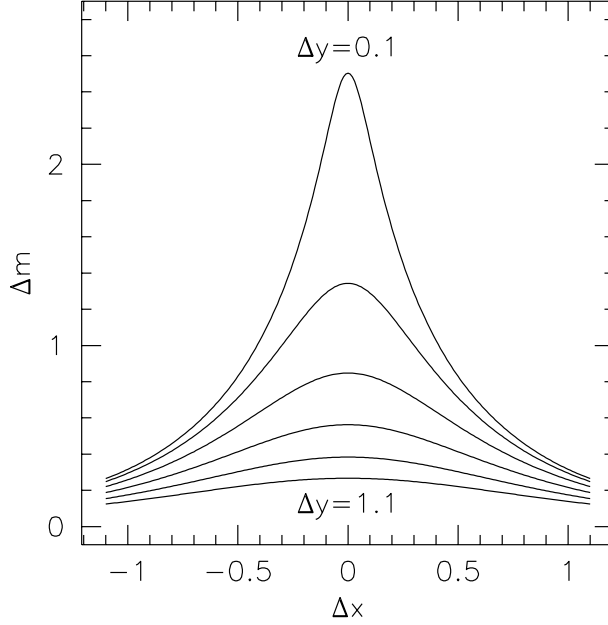


Figure 9: Microlensing-induced light curves for six minimum separations between the source and the lens, $\Delta y = 0.1, 0.3, \dots, 1.1$. The separation is expressed in units of the Einstein radius.

Fortunately, the light curves of lensed stars have certain tell-tale signatures — the light curves are expected to be symmetric in time and the magnification is expected to be achromatic because light deflection does not depend on wavelength (but see the more detailed discussion in Sect. 2.2.4 below). In contrast, intrinsically variable stars typically have asymmetric light curves and do change their colors.

The expected time scale for microlensing-induced variations is given in terms of the typical angular scale θ_E , the relative velocity v between source and lens, and the distance to the lens:

$$t_0 = \frac{D_d \theta_E}{v} = 0.214 \text{ yr} \left(\frac{M}{M_\odot} \right)^{1/2} \left(\frac{D_d}{10 \text{ kpc}} \right)^{1/2} \left(\frac{D_{ds}}{D_s} \right)^{1/2} \left(\frac{200 \text{ km s}^{-1}}{v} \right). \quad (30)$$

The ratio $D_{ds} D_s^{-1}$ is close to unity if the lenses are located in the Galactic halo and the sources are in the LMC. If light curves are sampled with time intervals between about an hour and a year, MACHOs in the mass range $10^{-6} M_\odot$ to $10^2 M_\odot$ are potentially detectable. Note that the measurement of t_0 in a given microlensing event does not directly give M , but only a combination of M , D_d , D_s , and v . Various ideas to break this degeneracy have been discussed. Figure 9 shows microlensing-induced light curves for six different minimum separations $\Delta y = u_{\min}$ between the source and the lens. The widths of the peaks are $\sim t_0$, and there is a direct one-to-one mapping between Δy and the maximum magnification at the peak of the light curve. A microlensing light curve therefore gives two observables, t_0 and Δy .

The chance of seeing a microlensing event is usually expressed in terms of the optical depth, which is the probability that at any instant of time a given star is within an angle θ_E of a lens. The optical depth is the integral over the number density $n(D_d)$ of lenses times the area enclosed by the Einstein ring of each lens, i.e.

$$\tau = \frac{1}{\delta\omega} \int dV n(D_d) \pi \theta_E^2, \quad (31)$$

where $dV = \delta\omega D_d^2 dD_d$ is the volume of an infinitesimal spherical shell with radius D_d which covers a solid angle $\delta\omega$. The integral gives the solid angle covered by the Einstein circles of the lenses, and the probability is obtained upon dividing this quantity by the solid angle $\delta\omega$ which is observed. Inserting equation (21) for the Einstein angle, we obtain

$$\tau = \int_0^{D_s} \frac{4\pi G\rho}{c^2} \frac{D_d D_{ds}}{D_s} dD_d = \frac{4\pi G}{c^2} D_s^2 \int_0^1 \rho(x) x(1-x) dx, \quad (32)$$

where $x \equiv D_d D_s^{-1}$ and ρ is the mass density of MACHOs. We have made use of the fact in (32) that space is locally Euclidean, hence $D_{ds} = D_s - D_d$. If ρ is constant along the line-of-sight, the optical depth simplifies to

$$\tau = \frac{2\pi}{3} \frac{G\rho}{c^2} D_s^2. \quad (33)$$

It is important to note that the optical depth τ depends on the *mass density* of lenses ρ and not on their *mass* M . The timescale of variability induced by microlensing, however, does depend on the square root of the mass, as shown in eq. (30).

2.2.2 Ongoing Galactic Microlensing Searches

Paczynski's suggestion that microlensing by compact objects in the Galactic halo may be detected by monitoring the light curves of stars in the LMC inspired several groups to set up elaborate searches for microlensing events. Four groups, MACHO (Alcock et al. 1993), EROS (Aubourg et al. 1993), OGLE (Udalski et al. 1992), and DUO (Alard 1995), are currently searching for microlensing-induced stellar variability in the LMC (EROS, MACHO) as well as in the Galactic bulge (DUO, MACHO, OGLE).

So far, about 100 microlensing events have been observed, and their number is increasing rapidly. Most events have been seen toward the Galactic bulge. The majority of events have been caused by single lenses, and have light curves similar to those shown in Fig. 9, but at least two events so far are due to binary lenses. Strong lensing by binaries (defined as events where the source crosses one or more caustics, see Fig. 10) was estimated by Mao & Paczyński (1991) to contribute about 10 per cent of all events. Binary lensing is most easily distinguished from single-lens events by characteristic double-peaked or asymmetric light curves; Fig. 10 shows some typical examples.

The light curve of the first observed binary microlensing event, OGLE #7, is shown in Fig. 11.

2.2.3 Early Results on Optical Depths

Both the OGLE and MACHO collaborations have determined the microlensing optical depth toward the Galactic bulge. The results are

$$\tau = \begin{cases} (3.3 \pm 1.2) \times 10^{-6} & \text{(Paczynski et al. 1994)} \\ (3.9_{-1.2}^{+1.8}) \times 10^{-6} & \text{(Alcock et al. 1996b)} \end{cases}. \quad (34)$$

Original theoretical estimates (Paczynski 1991; Griest, Alcock, & Axelrod 1991) had predicted an optical depth below 10^{-6} . Even though this value was increased slightly by Kiraga & Paczyński (1994) who realized the importance of lensing of background bulge stars by foreground bulge stars (referred to as self-lensing of the bulge), the measured optical depth is nevertheless very much higher than expected. Paczynski et al. (1994) suggested that a Galactic bar which is approximately aligned with the line-of-sight towards the Galactic bulge might explain the excess optical depth. Self-consistent calculations of the bar by Zhao, Spergel, & Rich (1995) give $\tau \sim 2 \times 10^{-6}$, which is within one standard deviation of the observed value. Zhao et al. (1995) also conclude that the duration distribution of the bulge events detected by OGLE is compatible with a roughly normal stellar mass distribution.

Based on three events from their first year of data, of which two are of only modest significance, Alcock et al. (1996a) estimated the optical depth toward the LMC to be

$$\tau = 9_{-5}^{+7} \times 10^{-8}, \quad (35)$$

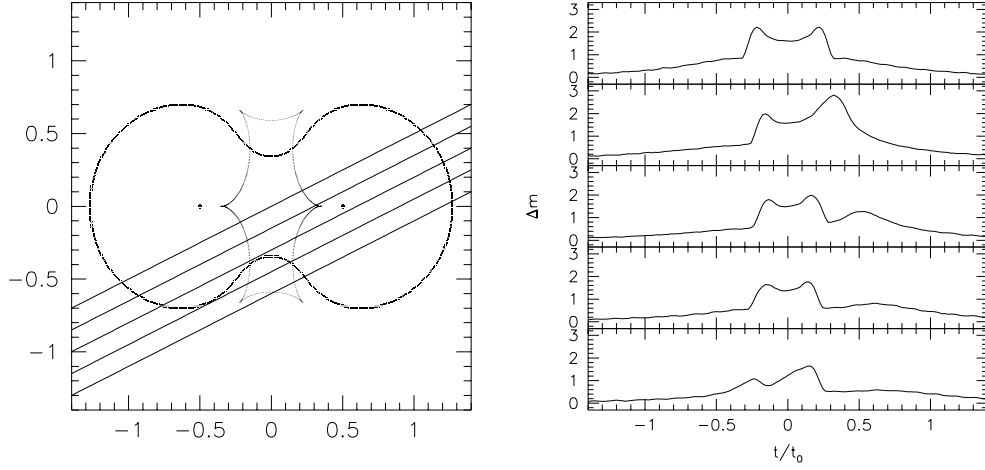


Figure 10: Left panel: A binary lens composed of two equal point masses. The critical curve is shown by the heavy line, and the corresponding caustic is indicated by the thin line with six cusps. (See Sect. 3.3.2 for a definition of critical curves and caustics.) Five source trajectories across this lens system are indicated. Right panel: Light curves corresponding to an extended source moving along the trajectories indicated in the left panel. Double-peaked features occur when the source comes close to both lenses.

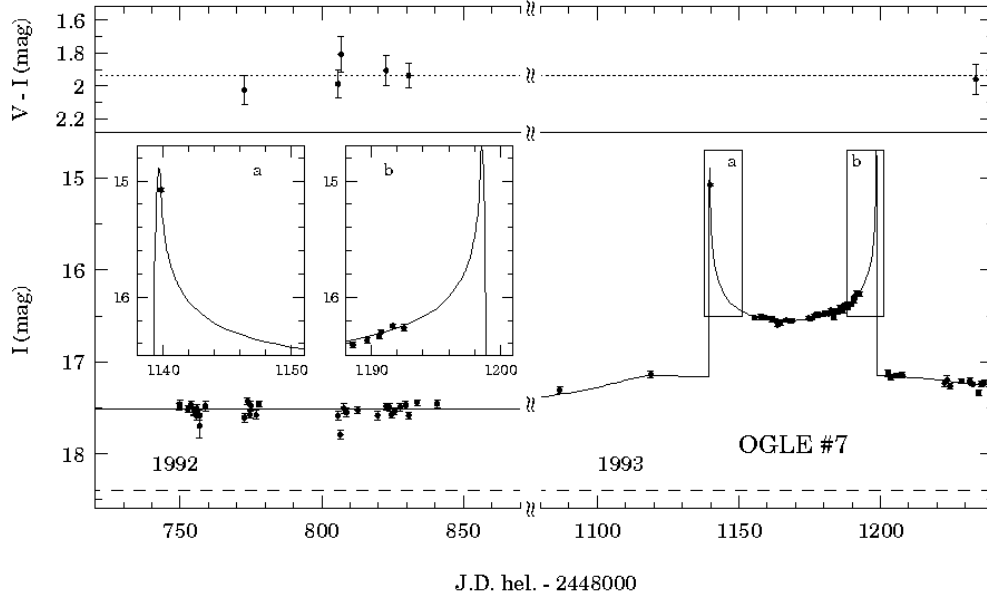


Figure 11: Light curve of the first binary microlensing event, OGLE #7 (taken from the OGLE WWW home page).

in the mass range $10^{-4} M_{\odot} < M < 10^{-1} M_{\odot}$. This is too small for the entire halo to be made of MACHOs in this mass range. At the 95% confidence level, the first-year data of the MACHO collaboration rule out a contribution from MACHOs to the halo mass $\gtrsim 40\%$ in the mass range $10^{-3} M_{\odot} \leq M \leq 10^{-2} M_{\odot}$, and $\gtrsim 60\%$ within $10^{-4} M_{\odot} \leq M \leq 10^{-1} M_{\odot}$. Sahu (1994) argued that all events can be due to objects in the Galactic disk or the LMC itself. The EROS collaboration, having better time resolution, is able to probe smaller masses, $10^{-7} M_{\odot} \leq M \leq 10^{-1} M_{\odot}$ (Aubourg et al. 1995). The 95% confidence level from the EROS data excludes a halo fraction $\gtrsim (20 - 30)\%$ in the mass range $10^{-7} M_{\odot} \leq M \leq 10^{-2} M_{\odot}$ (Ansari et al. 1996; see also Roulet & Mollerach 1996).

More recently, the MACHO group reported results from their second year of data. Based on 6 to 8 events, they now estimate the halo fraction to be $0.3 - 0.9$ in the mass range $0.1 M_{\odot} \leq M \leq 0.4 M_{\odot}$ at 68% confidence. Further, they cannot reject, at the 99% confidence level, the hypothesis that the entire halo is made of MACHOs with masses $0.2 M_{\odot} \leq M \leq 1 M_{\odot}$ (Bennett 1996). More data are needed before any definitive conclusion can be reached on the contribution of MACHOs to the halo.

2.2.4 Other Interesting Discoveries

In the simplest scenario of microlensing in the Galaxy, a single point-like source is lensed by a single point mass which moves with constant velocity relative to the source. The light curve observed from such an event is time-symmetric and achromatic. At the low optical depths that we expect in the Galaxy, and ignoring binaries, microlensing events should not repeat since the probability that the same star is lensed more than once is negligibly small.

In practice, the situation is more complicated and detailed interpretations of observed light curves must account for some of the complications listed below. The effects of binary lenses have already been mentioned above. In the so-called *resonant* case, the separation of the two lenses is comparable to their Einstein radii. The light curve of such a lens system can have dramatic features such as the double peaks shown in Figs. 10 and 11. At least two such events have been observed so far, OGLE #7 (Udalski et al. 1994; Bennett et al. 1995) and DUO #2 (Alard, Mao, & Guibert 1995). In the non-resonant case, the lenses are well separated and act as almost independent lenses. Di Stefano & Mao (1996) estimated that a few per cent of all microlensing events should “repeat” due to consecutive magnification of a star by the two stars in a wide binary lens.

The sensitivity of microlensing searches to binaries may make this a particularly powerful method to search for planets around distant stars, as emphasized by Mao & Paczyński (1991) and Gould & Loeb (1992).

Multiple sources can give rise to various other complications. Since the optical depth is low, microlensing searches are performed in crowded fields where the number density of sources is high. Multiple source stars which are closer to each other than $\sim 1''$ appear as single because they are not resolved. The Einstein radius of a solar mass lens, on the other hand, is $\sim (10^{-3})''$ (cf. eq. 22). Therefore, if the projected separation of two sources is $< 1''$ but $> (10^{-3})''$, a single lens affects only one of them at a time. Several effects can then occur. First, the microlensing event can apparently recur when the two sources are lensed individually (Griest & Hu 1992). Second, if the sources have different colors, the event is chromatic because the color of the lensed star dominates during the event (Udalski et al. 1994; Kamionkowski 1995). Third, the observed flux is a blend of the magnified flux from the lensed component and the constant flux of the unlensed components, and this leads to various biases (Di Stefano & Esin 1995). A systematic method of detecting microlensing in blended data has been proposed and is referred to as “pixel lensing” (Crotts 1992; Baillon et al. 1993; Colley 1995).

Stars are not truly point-like. If a source is larger than the impact parameter of a single lens or the caustic structure of a binary lens, the finite source size modifies the light curve significantly (Gould 1994a; Nemiroff & Wickramasinghe 1994; Witt & Mao 1994; Witt 1995).

Finally, if the relative transverse velocity of the source, the lens, and the observer is not constant during the event, the light curve becomes time-asymmetric. The parallax effect due

to the acceleration of the Earth was predicted by Gould (1992b) and detected by Alcock et al. (1995b). The detection of parallax provides an additional observable which helps partially to break the degeneracy among M , v , D_d and D_{ds} mentioned in Sect. 2.2.1.

Another method of breaking the degeneracy is via observations from space. The idea of space measurements was suggested by Refsdal as early as 1966 as a means to determine distances and masses of lenses in the context of quasar lensing (Refsdal 1966b). Some obvious benefits of space-based telescopes include absence of seeing and access to wavebands like the UV or IR which are absorbed by the Earth's atmosphere. The particular advantage of space observations for microlensing in the Galaxy arises from the fact that the Einstein radius of a sub-solar mass microlens in the Galactic halo is of order 10^8 km and thus comparable to the AU, cf. eq. (22). Telescopes separated by ~ 1 AU would therefore observe different light curves for the same microlensing event. This additional information on the event can break the degeneracy between the parameters defining the time scale t_0 (Gould 1994b). In the special (and rare) case of very high magnification when the source is resolved during the event (Gould 1994a), all four parameters may be determined.

Interesting discoveries can be expected from the various microlensing “alert systems” which have been recently set up (GMAN, Pratt 1996; PLANET, Sackett 1996). The goal of these is to monitor ongoing microlensing events in almost real time with very high time resolution. It should be possible to detect anomalies in the microlensing lightcurves which are expected from the complications listed in this section, or to obtain detailed information (e.g. spectra, Sahu 1996) from objects while they are being microlensed.

2.3 Extragalactic Microlenses

2.3.1 Point Masses in the Universe

It has been proposed at various times that a significant fraction of the dark matter in the universe may be in the form of compact masses. These masses will induce various lensing phenomena, some of which are very easily observed. The lack of evidence for these phenomena can therefore be used to place useful limits on the fraction of the mass in the universe in such objects (Press & Gunn 1973).

Consider an Einstein-de Sitter universe with a constant comoving number density of point lenses of mass M corresponding to a cosmic density parameter Ω_M . The optical depth for lensing of sources at redshift z_s can be shown to be

$$\begin{aligned}\tau(z_s) &= 3\Omega_M \left[\frac{(z_s + 2 + 2\sqrt{1+z_s}) \ln(1+z_s)}{z_s} - 4 \right] \\ &\simeq \Omega_M \frac{z_s^2}{4} \quad \text{for } z_s \ll 1 \\ &\simeq 0.3\Omega_M \quad \text{for } z_s = 2.\end{aligned}\tag{36}$$

We see that the probability for lensing is $\sim \Omega_M$ for high-redshift sources (Press & Gunn 1973). Hence the number of lensing events in a given source sample directly measures the cosmological density in compact objects.

In calculating the probability of lensing it is important to allow for various selection effects. Lenses magnify the observed flux, and therefore sources which are intrinsically too faint to be observed may be lifted over the detection threshold. At the same time, lensing increases the solid angle within which sources are observed so that their number density in the sky is reduced (Narayan 1991). If there is a large reservoir of faint sources, the increase in source number due to the apparent brightening outweighs their spatial dilution, and the observed number of sources is increased due to lensing. This magnification bias (Turner 1980; Turner, Ostriker, & Gott 1984; Narayan & Wallington 1993) can substantially increase the probability of lensing for bright optical quasars whose number-count function is steep.

Table 1: Summary of techniques to constrain Ω_M in point masses, along with the current best limits.

Technique	References	Mass Range M_\odot	Limit on Ω_M
Image doubling of bright QSOs	Surdej et al. (1993)	$10^{10} - 10^{12}$	< 0.02
Doubling of VLBI compact sources	Kassiola et al. (1991) Henstock et al. (1995)	$10^6 - 10^8$	< 0.05
Echoes from γ -ray bursts	Nemiroff et al. (1993) Nemiroff et al. (1994)	$10^{6.5} - 10^{8.1}$ $(10^3 \rightarrow)$	$\lesssim 1$ excluded null result
Diff. magnification of QSO continuum vs. broad emission lines	Canizares (1982) Dalcanton et al. (1994)	$10^{-1} - 20$ $10^{-3} - 60$	< 0.1 < 0.2
Quasar variability	Schneider (1993)	$10^{-3} - 10^{-2}$	< 0.1
Femtolensing of γ -ray bursts	Gould (1992a) Stanek et al. (1993)	$10^{-17} - 10^{-13}$	– –

2.3.2 Current Upper Limits on Ω_M in Point Masses

Various techniques have been proposed and applied to obtain limits on Ω_M over a broad range of lens masses (see Carr 1994 for a review). Lenses with masses in the range $10^{10} < M/M_\odot < 10^{12}$ will split images of bright QSOs by $0.3'' - 3''$. Such angular splittings are accessible to optical observations; therefore, it is easy to constrain Ω_M in this mass range. The image splitting of lenses with $10^6 < M/M_\odot < 10^8$ is on the order of milliarcseconds and falls within the resolution domain of VLBI observations of radio quasars (Kassiola, Kovner, & Blandford 1991). The best limits presently are due to Henstock et al. (1995). A completely different approach utilizes the differential time delay between multiple images. A cosmological γ -ray burst, which is gravitationally lensed will be seen as multiple repetitions of a single event (Blaes & Webster 1992). By searching the γ -ray burst database for (lack of) evidence of repetitions, Ω_M can be constrained over a range of masses which extends below the VLBI range mentioned above. The region within QSOs where the broad emission lines are emitted is larger than the region emitting the continuum radiation. Lenses with $M \sim 1 M_\odot$ can magnify the continuum relative to the broad emission lines and thereby reduce the observed emission line widths. Lenses of still smaller masses cause apparent QSO variability, and hence from observations of the variability an upper limit to Ω_M can be derived. Finally, the time delay due to lenses with very small masses can be such that the light beams from multiply imaged γ -ray bursts interfere so that the observed burst spectra should show interference patterns. Table 1 summarizes these various techniques and gives the most recent results on Ω_M .

As Table 1 shows, we can eliminate $\Omega_M \sim 1$ in virtually all astrophysically plausible mass ranges. The limits are especially tight in the range $10^6 < M/M_\odot < 10^{12}$, where Ω_M is constrained to be less than a few per cent.

2.3.3 Microlensing in QSO 2237+0305

Although the Galactic microlensing projects described earlier have developed into one of the most exciting branches of gravitational lensing, the phenomenon of microlensing was in fact first detected in a cosmological source, the quadruply-imaged QSO 2237+0305 (Irwin et al. 1989; Corrigan et al. 1991; Webster et al. 1991; Østensen et al. 1996). The lensing galaxy in QSO 2237+0305 is a spiral at a redshift of 0.04 (Huchra et al. 1985). The four quasar images are almost symmetrically located in a cross-shaped pattern around the nucleus of the galaxy; hence the system has been named the ‘‘Einstein Cross’’. Uncorrelated flux variations have been observed in QSO 2237+0305,

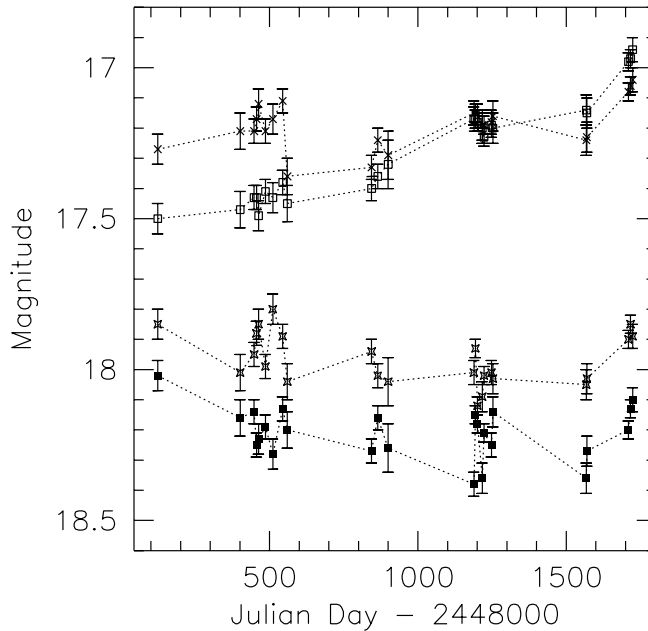


Figure 12: Light curves of the four images in the “Einstein Cross” QSO 2237+0305 since August 1990 (from Østensen et al. 1996)

possibly in all four images, and these variations provide evidence for microlensing due to stars in the lensing galaxy. Figure 12 shows the light curves of the four images.

The interpretation of the microlensing events in QSO 2237+0305 is much less straightforward than in the case of microlensing in the Galaxy. When a distant galaxy forms multiple images, the surface mass density at the locations of the images is of order the critical density, Σ_{cr} . If most of the local mass is made of stars or other massive compact objects (as is likely in the case of QSO 2237+0305 since the four images are superposed on the bulge of the lensing spiral galaxy), the optical depth to microlensing approaches unity. In such a case, the mean projected separation of the stars is comparable to or smaller than their Einstein radii, and the effects of the various microlenses cannot be considered independently. Complicated caustic networks arise (Paczynski 1986a; Schneider & Weiss 1987; Wambsganss 1990), and the observed light curves have to be analyzed statistically on the basis of numerical simulations. A new and elegant method to compute microlensing light curves of point sources was introduced by Witt (1993).

Two important conclusions have been drawn from the microlensing events in QSO 2237+0305. First, it has been shown that the continuum emitting region in QSO 2237+0305 must have a size $\sim 10^{15}$ cm (Wambsganss, Paczynski, & Schneider 1990; Rauch & Blandford 1991) in order to produce the observed amplitude of magnification fluctuations. This is the most direct and stringent limit yet on the size of an optical QSO. Second, it appears that the mass spectrum of microlenses in the lensing galaxy is compatible with a normal mass distribution similar to that observed in our own Galaxy (Seitz, Wambsganss, & Schneider 1994).

3 Lensing by Galaxies

Lensing by point masses, the topic we have considered so far, is particularly straightforward because of the simplicity of the lens. When we consider galaxy lenses we need to allow for the

distributed nature of the mass, which is usually done via a parameterized model. The level of complexity of the model is dictated by the application at hand.

3.1 Lensing by a Singular Isothermal Sphere

A simple model for the mass distribution in galaxies assumes that the stars and other mass components behave like particles of an ideal gas, confined by their combined, spherically symmetric gravitational potential. The equation of state of the “particles”, henceforth called stars for simplicity, takes the form

$$p = \frac{\rho kT}{m} , \quad (37)$$

where ρ and m are the mass density and the mass of the stars. In thermal equilibrium, the temperature T is related to the one-dimensional velocity dispersion σ_v of the stars through

$$m\sigma_v^2 = kT . \quad (38)$$

The temperature, or equivalently the velocity dispersion, could in general depend on radius r , but it is usually assumed that the stellar gas is isothermal, so that σ_v is constant across the galaxy. The equation of hydrostatic equilibrium then gives

$$\frac{p'}{\rho} = -\frac{GM(r)}{r^2} , \quad M'(r) = 4\pi r^2 \rho , \quad (39)$$

where $M(r)$ is the mass interior to radius r , and primes denote derivatives with respect to r . A particularly simple solution of eqs. (37) through (39) is

$$\rho(r) = \frac{\sigma_v^2}{2\pi G} \frac{1}{r^2} . \quad (40)$$

This mass distribution is called the *singular isothermal sphere*. Since $\rho \propto r^{-2}$, the mass $M(r)$ increases $\propto r$, and therefore the rotational velocity of particles in the gravitational field of the singular isothermal sphere is

$$v_{\text{rot}}^2(r) = \frac{GM(r)}{r} = 2\sigma_v^2 = \text{constant} . \quad (41)$$

The flat rotation curves of galaxies are naturally reproduced by this model.

Upon projecting along the line-of-sight, we obtain the surface mass density

$$\Sigma(\xi) = \frac{\sigma_v^2}{2G} \frac{1}{\xi} , \quad (42)$$

where ξ is the distance from the center of the two-dimensional profile. Referring to eq. (11), we immediately obtain the deflection angle

$$\hat{\alpha} = 4\pi \frac{\sigma_v^2}{c^2} = (1.4'') \left(\frac{\sigma_v}{220 \text{ km s}^{-1}} \right)^2 , \quad (43)$$

which is independent of ξ and points toward the center of the lens. The Einstein radius of the singular isothermal sphere follows from eq. (20),

$$\theta_E = 4\pi \frac{\sigma_v^2}{c^2} \frac{D_{\text{ds}}}{D_s} = \hat{\alpha} \frac{D_{\text{ds}}}{D_s} = \alpha . \quad (44)$$

Due to circular symmetry, the lens equation is essentially one-dimensional. Multiple images are obtained only if the source lies inside the Einstein ring, i.e. if $\beta < \theta_E$. When this condition is satisfied, the lens equation has the two solutions

$$\theta_{\pm} = \beta \pm \theta_E . \quad (45)$$

The images at θ_{\pm} , the source, and the lens all lie on a straight line. Technically, a third image with zero flux is located at $\theta = 0$. This third image acquires a finite flux if the singularity at the center of the lens is replaced by a core region with a finite density.

The magnifications of the two images follow from eq. (26),

$$\mu_{\pm} = \frac{\theta_{\pm}}{\beta} = 1 \pm \frac{\theta_E}{\beta} = \left(1 \mp \frac{\theta_E}{\theta_{\pm}}\right)^{-1}. \quad (46)$$

If the source lies outside the Einstein ring, i.e. if $\beta > \theta_E$, there is only one image at $\theta = \theta_+ = \beta + \theta_E$.

3.2 Effective Lensing Potential

Before proceeding to other galaxy lens models, it is useful to develop the formalism a little further. Let us define a scalar potential $\psi(\vec{\theta})$ which is the appropriately scaled, projected Newtonian potential of the lens,

$$\psi(\vec{\theta}) = \frac{D_{\text{ds}}}{D_{\text{d}} D_{\text{s}}} \frac{2}{c^2} \int \Phi(D_{\text{d}} \vec{\theta}, z) dz. \quad (47)$$

The derivatives of ψ with respect to $\vec{\theta}$ have convenient properties. The gradient of ψ with respect to θ is the deflection angle,

$$\vec{\nabla}_{\theta} \psi = D_{\text{d}} \vec{\nabla}_{\xi} \psi = \frac{2}{c^2} \frac{D_{\text{ds}}}{D_{\text{s}}} \int \vec{\nabla}_{\perp} \Phi dz = \vec{\alpha}, \quad (48)$$

while the Laplacian is proportional to the surface-mass density Σ ,

$$\nabla_{\theta}^2 \psi = \frac{2}{c^2} \frac{D_{\text{d}} D_{\text{ds}}}{D_{\text{s}}} \int \nabla_{\xi}^2 \Phi dz = \frac{2}{c^2} \frac{D_{\text{d}} D_{\text{ds}}}{D_{\text{s}}} \cdot 4\pi G \Sigma = 2 \frac{\Sigma(\vec{\theta})}{\Sigma_{\text{cr}}} \equiv 2\kappa(\vec{\theta}), \quad (49)$$

where Poisson's equation has been used to relate the Laplacian of Φ to the mass density. The surface mass density scaled with its critical value Σ_{cr} is called the *convergence* $\kappa(\vec{\theta})$. Since ψ satisfies the two-dimensional Poisson equation $\nabla_{\theta}^2 \psi = 2\kappa$, the effective lensing potential can be written in terms of κ

$$\psi(\vec{\theta}) = \frac{1}{\pi} \int \kappa(\vec{\theta}') \ln |\vec{\theta} - \vec{\theta}'| d^2 \theta'. \quad (50)$$

As mentioned earlier, the deflection angle is the gradient of ψ , hence

$$\vec{\alpha}(\vec{\theta}) = \vec{\nabla} \psi = \frac{1}{\pi} \int \kappa(\vec{\theta}') \frac{\vec{\theta} - \vec{\theta}'}{|\vec{\theta} - \vec{\theta}'|^2} d^2 \theta', \quad (51)$$

which is equivalent to eq. (10) if we account for the definition of Σ_{cr} given in eq. (17).

The local properties of the lens mapping are described by its Jacobian matrix \mathcal{A} ,

$$\mathcal{A} \equiv \frac{\partial \vec{\beta}}{\partial \vec{\theta}} = \left(\delta_{ij} - \frac{\partial \alpha_i(\vec{\theta})}{\partial \theta_j} \right) = \left(\delta_{ij} - \frac{\partial^2 \psi(\vec{\theta})}{\partial \theta_i \partial \theta_j} \right) = \mathcal{M}^{-1}. \quad (52)$$

As we have indicated, \mathcal{A} is nothing but the inverse of the magnification tensor \mathcal{M} . The matrix \mathcal{A} is therefore also called the inverse magnification tensor. The local solid-angle distortion due to the lens is given by the determinant of \mathcal{A} . A solid-angle element $\delta\beta^2$ of the source is mapped to the solid-angle element of the image $\delta\theta^2$, and so the magnification is given by

$$\frac{\delta\theta^2}{\delta\beta^2} = \det \mathcal{M} = \frac{1}{\det \mathcal{A}}. \quad (53)$$

This expression is the appropriate generalization of eq. (26) when there is no symmetry.

Equation (52) shows that the matrix of second partial derivatives of the potential ψ (the Hessian matrix of ψ) describes the deviation of the lens mapping from the identity mapping. For convenience, we introduce the abbreviation

$$\frac{\partial^2 \psi}{\partial \theta_i \partial \theta_j} \equiv \psi_{ij} . \quad (54)$$

Since the Laplacian of ψ is twice the convergence, we have

$$\kappa = \frac{1}{2} (\psi_{11} + \psi_{22}) = \frac{1}{2} \text{tr} \psi_{ij} . \quad (55)$$

Two additional linear combinations of ψ_{ij} are important, and these are the components of the *shear* tensor,

$$\begin{aligned} \gamma_1(\vec{\theta}) &= \frac{1}{2} (\psi_{11} - \psi_{22}) \equiv \gamma(\vec{\theta}) \cos [2\phi(\vec{\theta})] , \\ \gamma_2(\vec{\theta}) &= \psi_{12} = \psi_{21} \equiv \gamma(\vec{\theta}) \sin [2\phi(\vec{\theta})] . \end{aligned} \quad (56)$$

With these definitions, the Jacobian matrix can be written

$$\begin{aligned} \mathcal{A} &= \begin{pmatrix} 1 - \kappa - \gamma_1 & -\gamma_2 \\ -\gamma_2 & 1 - \kappa + \gamma_1 \end{pmatrix} \\ &= (1 - \kappa) \begin{pmatrix} 1 & 0 \\ 0 & 1 \end{pmatrix} - \gamma \begin{pmatrix} \cos 2\phi & \sin 2\phi \\ \sin 2\phi & -\cos 2\phi \end{pmatrix} . \end{aligned} \quad (57)$$

The meaning of the terms convergence and shear now becomes intuitively clear. Convergence acting alone causes an isotropic focusing of light rays, leading to an isotropic magnification of a source. The source is mapped onto an image with the same shape but larger size. Shear introduces anisotropy (or astigmatism) into the lens mapping; the quantity $\gamma = (\gamma_1^2 + \gamma_2^2)^{1/2}$ describes the magnitude of the shear and ϕ describes its orientation. As shown in Fig. 13, a circular source of unit radius becomes, in the presence of both κ and γ , an elliptical image with major and minor axes

$$(1 - \kappa - \gamma)^{-1} , \quad (1 - \kappa + \gamma)^{-1} . \quad (58)$$

The magnification is

$$\mu = \det \mathcal{M} = \frac{1}{\det \mathcal{A}} = \frac{1}{[(1 - \kappa)^2 - \gamma^2]} . \quad (59)$$

Note that the Jacobian \mathcal{A} is in general a function of position $\vec{\theta}$.

3.3 Gravitational Lensing via Fermat's Principle

3.3.1 The Time-Delay Function

The lensing properties of model gravitational lenses are especially easy to visualize by application of Fermat's principle of geometrical optics (Nityananda 1984, unpublished; Schneider 1985; Blandford & Narayan 1986; Nityananda & Samuel 1992). From the lens equation (14) and the fact that the deflection angle is the gradient of the effective lensing potential ψ , we obtain

$$(\vec{\theta} - \vec{\beta}) - \vec{\nabla}_{\theta} \psi = 0 . \quad (60)$$

This equation can be written as a gradient,

$$\vec{\nabla}_{\theta} \left[\frac{1}{2} (\vec{\theta} - \vec{\beta})^2 - \psi \right] = 0 . \quad (61)$$

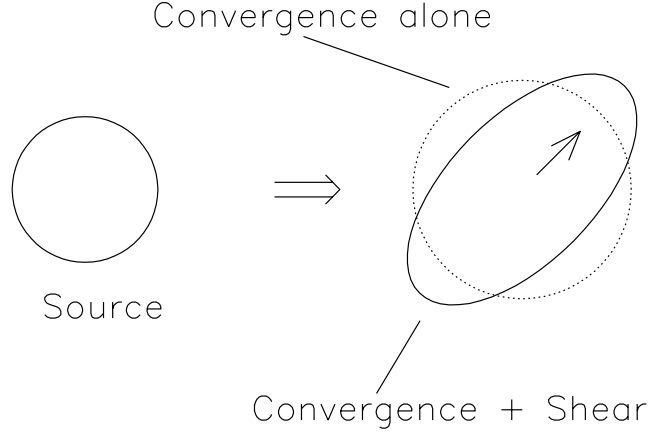


Figure 13: Illustration of the effects of convergence and shear on a circular source. Convergence magnifies the image isotropically, and shear deforms it to an ellipse.

The physical meaning of the term in square brackets becomes more obvious by considering the time-delay function,

$$\begin{aligned}
 t(\vec{\theta}) &= \frac{(1+z_d)}{c} \frac{D_d D_s}{D_{ds}} \left[\frac{1}{2} (\vec{\theta} - \vec{\beta})^2 - \psi(\vec{\theta}) \right] \\
 &= t_{\text{geom}} + t_{\text{grav}} .
 \end{aligned}
 \tag{62}$$

The term t_{geom} is proportional to the square of the angular offset between $\vec{\beta}$ and $\vec{\theta}$ and is the time delay due to the extra path length of the deflected light ray relative to an unperturbed null geodesic. The coefficient in front of the square brackets ensures that the quantity corresponds to the time delay as measured by the observer. The second term t_{grav} is the time delay due to gravity and is identical to the Shapiro delay introduced in eq. (3), with an extra factor of $(1+z_d)$ to allow for time stretching. Equations (61) and (62) imply that images satisfy the condition $\vec{\nabla}_{\theta} t(\vec{\theta}) = 0$.

In the case of a circularly symmetric deflector, the source, the lens and the images have to lie on a straight line on the sky. Therefore, it is sufficient to consider the section along this line of the time delay function. Figure 14 illustrates the geometrical and gravitational time delays for this case. The top panel shows t_{geom} for a slightly offset source. The curve is a parabola centered on the position of the source. The central panel displays t_{grav} for an isothermal sphere with a softened core. This curve is centered on the lens. The bottom panel shows the total time-delay. According to the above discussion images are located at stationary points of $t(\theta)$. For the case shown in Fig. 14 there are three stationary points, marked by dots, and the corresponding values of θ give the image positions.

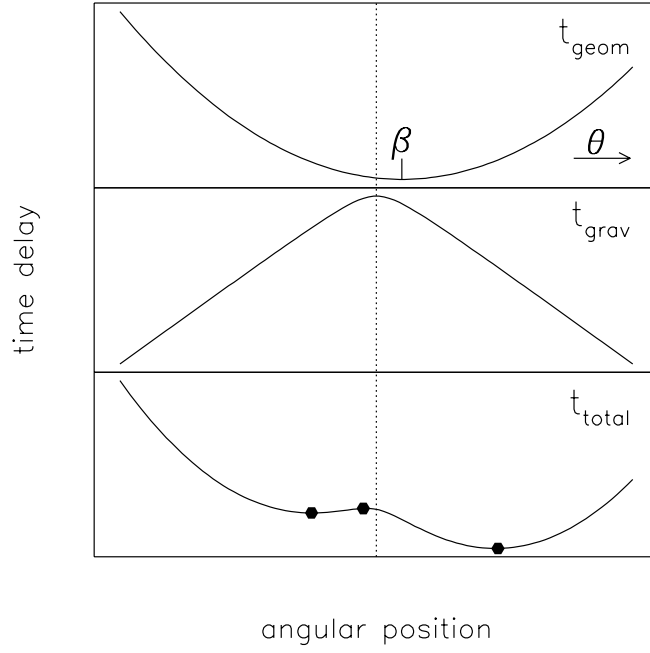


Figure 14: Geometric, gravitational, and total time delay of a circularly symmetric lens for a source that is slightly offset from the symmetry axis. The dotted line shows the location of the center of the lens, and β shows the position of the source. Images are located at points where the total time delay function is stationary. The image positions are marked with dots in the bottom panel.

3.3.2 Properties of the Time-Delay Function

In the general case it is necessary to consider image locations in the two-dimensional space of $\vec{\theta}$, not just on a line. The images are then located at those points $\vec{\theta}_i$ where the two-dimensional time-delay surface $t(\vec{\theta})$ is stationary. This is *Fermat's Principle* in geometrical optics, which states that the actual trajectory followed by a light ray is such that the light-travel time is stationary relative to neighboring trajectories. The time-delay surface $t(\vec{\theta})$ has a number of useful properties.

- 1 The height difference between two stationary points on $t(\vec{\theta})$ gives the relative time delay between the corresponding images. Any variability in the source is observed first in the image corresponding to the lowest point on the surface, followed by the extrema located at successively larger values of t . In Fig. 14 for instance, the first image to vary is the one that is farthest from the center of the lens. Although Fig. 14 corresponds to a circularly symmetric lens, this property usually carries over even for lenses that are not perfectly circular. Thus, in QSO 0957+561, we expect the A image, which is $\sim 5''$ from the lensing galaxy, to vary sooner than the B image, which is only $\sim 1''$ from the center. This is indeed observed (for recent optical and radio light curves of QSO 0957+561 see Schild & Thomson 1993 and Haarsma et al. 1996).
- 2 There are three types of stationary points of a two-dimensional surface: minima, saddle points, and maxima. The nature of the stationary points is characterized by the eigenvalues of the Hessian matrix of the time-delay function at the location of the stationary points

$$\mathcal{T} = \frac{\partial^2 t(\vec{\theta})}{\partial \theta_i \partial \theta_j} \propto (\delta_{ij} - \psi_{ij}) = \mathcal{A}. \quad (63)$$

The matrix \mathcal{T} describes the local curvature of the time-delay surface. If both eigenvalues of \mathcal{T} are positive, $t(\vec{\theta})$ is curved “upward” in both coordinate directions, and the stationary point is a minimum. If the eigenvalues of \mathcal{T} have opposite signs we have a saddle point, and if both eigenvalues of \mathcal{T} are negative, we have a maximum. Correspondingly, we can distinguish three types of images. Images of type I arise at minima of $t(\vec{\theta})$ where $\det \mathcal{A} > 0$ and $\text{tr } \mathcal{A} > 0$. Images of type II are formed at saddle points of $t(\vec{\theta})$ where the eigenvalues have opposite signs, hence $\det \mathcal{A} < 0$. Images of type III are located at maxima of $t(\vec{\theta})$ where both eigenvalues are negative and so $\det \mathcal{A} > 0$ and $\text{tr } \mathcal{A} < 0$.

- 3 Since the magnification is the inverse of $\det \mathcal{A}$, images of types I and III have positive magnification and images of type II have negative magnification. The interpretation of a negative μ is that the parity of the image is reversed. A little thought shows that the three images shown in Fig. 14 correspond, from the left, to a saddle-point, a maximum and a minimum, respectively. The images A and B in QSO 0957+561 correspond to the images on the right and left in this example, and ought to represent a minimum and a saddle-point respectively in the time delay surface. VLBI observations do indeed show the expected reversal of parity between the two images (Gorenstein et al. 1988).
- 4 The curvature of $t(\vec{\theta})$ measures the inverse magnification. When the curvature of $t(\vec{\theta})$ along one coordinate direction is small, the image is strongly magnified along that direction, while if $t(\vec{\theta})$ has a large curvature the magnification is small. Figure 15 displays the time-delay function of a typical circularly symmetric lens and a source on the symmetry axis (top panel), a slightly offset source (central panel), and a source with a large offset (bottom panel). If the separation between source and lens is large, only one image is formed, while if the source is close to the lens three images are formed. Note that, as the source moves, two images approach each other, merge and vanish. It is easy to see that, quite generally, the curvature of $t(\theta)$ goes to zero as the images approach each other; in fact, the curvature varies as $\Delta\theta^{-1}$. Thus, we expect that the brightest image configurations are obtained when a pair of images are close together, just prior to merging. The lines in $\vec{\theta}$ -space on which images merge are

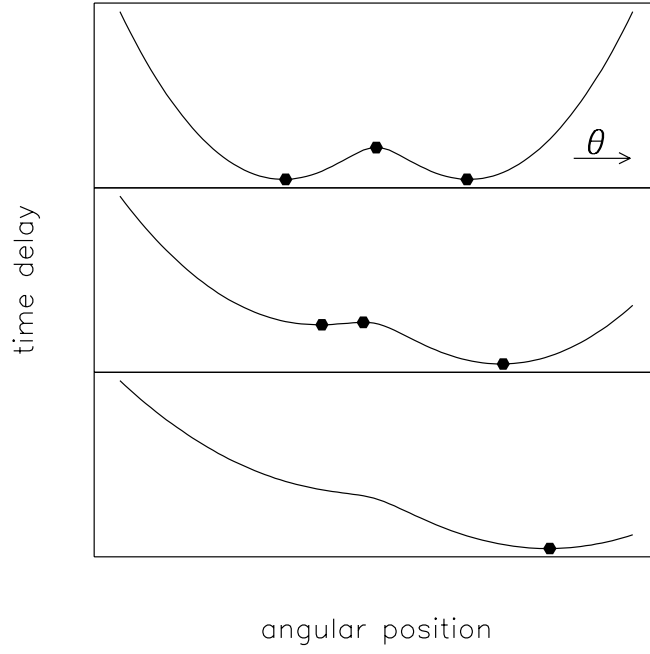


Figure 15: The time delay function of a circularly symmetric lens for a source exactly behind the lens (top panel), a source offset from the lens by a moderate angle (center panel) and a source offset by a large angle (bottom panel).

Table 2: Examples of circularly symmetric lenses. The effective lensing potential $\psi(\theta)$ and the deflection angle $\alpha(\theta)$ are given. The core radius of the softened isothermal sphere is θ_c .

Lens Model	$\psi(\theta)$	$\alpha(\theta)$
Point mass	$\frac{D_{\text{ds}}}{D_s} \frac{4GM}{D_d c^2} \ln \theta $	$\frac{D_{\text{ds}}}{D_s} \frac{4GM}{c^2 D_d \theta }$
Singular isothermal sphere	$\frac{D_{\text{ds}}}{D_s} \frac{4\pi\sigma^2}{c^2} \theta $	$\frac{D_{\text{ds}}}{D_s} \frac{4\pi\sigma^2}{c^2}$
Softened isothermal sphere	$\frac{D_{\text{ds}}}{D_s} \frac{4\pi\sigma^2}{c^2} (\theta_c^2 + \theta^2)^{1/2}$	$\frac{D_{\text{ds}}}{D_s} \frac{4\pi\sigma^2}{c^2} \frac{\theta}{(\theta_c^2 + \theta^2)^{1/2}}$
Constant density sheet	$\frac{\kappa}{2} \theta^2$	$\kappa \theta $

referred to as *critical lines*, while the corresponding source positions in $\vec{\beta}$ -space are called *caustics*. Critical lines and caustics are important because (i) they highlight regions of high magnification, and (ii) they demarcate regions of different image multiplicity. (The reader is referred to Blandford & Narayan 1986 and Erdl & Schneider 1992 for more details.)

- 5 When the source is far from the lens, we expect only a single image, corresponding to a minimum of the time delay surface. New extrema are always created in pairs (e.g. Fig. 15). Therefore, the total number of extrema, and thus the number of images of a generic (non-singular) lens, is odd (Burke 1981).

3.4 Circularly Symmetric Lens Models

Table 2 compiles formulae for the effective lensing potential and deflection angle of four commonly used circularly symmetric lens models; point mass, singular isothermal sphere, isothermal sphere with a softened core, and constant density sheet. In addition, one can have more general models with non-isothermal radial profiles, e.g. density varying as radius to a power other than -2 .

The gravitational time-delay functions $t_{\text{grav}}(\theta) \propto -\psi(\theta)$ of the models in Table 2 are illustrated in Fig. 16. Note that the four potentials listed in Tab. 2 all are divergent for $\theta \rightarrow \infty$. (Although the three-dimensional potential of the point mass drops $\propto r^{-1}$, its projection along the line-of-sight diverges logarithmically.) The divergence is, however, not serious since images always occur at finite θ where the functions are well-behaved.

The image configurations produced by a circularly symmetric lens are easily discovered by drawing time delay functions $t(\theta)$ as in Fig. 15 corresponding to various offsets of the source with respect to the lens. Figures 17 and 18 show typical image configurations. The right halves of the figures display the source plane, and the left halves show the image configuration in the lens plane. Since \mathcal{A} is a 2×2 matrix, a typical circularly symmetric lens has two critical lines where $\det \mathcal{A}$ vanishes, and two corresponding caustics in the source plane. The caustic of the outer critical curve degenerates to a critical point because of the circular symmetry of the lens. A source which is located outside the outermost caustic has a single image. Upon each caustic crossing, the image number changes by two, indicated by the numbers in Fig. 17. The three images of the source indicated as a small rectangle are marked in the left half of Fig. 17. The innermost image is usually very faint; in fact it vanishes if the lens has a singular core (the curvature of the time delay function then becomes infinite) as in the point mass or the singular isothermal sphere.

Figure 18 shows the images of two extended sources lensed by the same model as in Fig. 17. One source is located close to the point-like caustic in the center of the lens. It is imaged onto the two long, tangentially oriented arcs close to the outer critical curve and the very faint image at the lens center. The other source on the outer caustic forms a radially elongated image which is composed of two merging images, and a third tangentially oriented image outside the outer

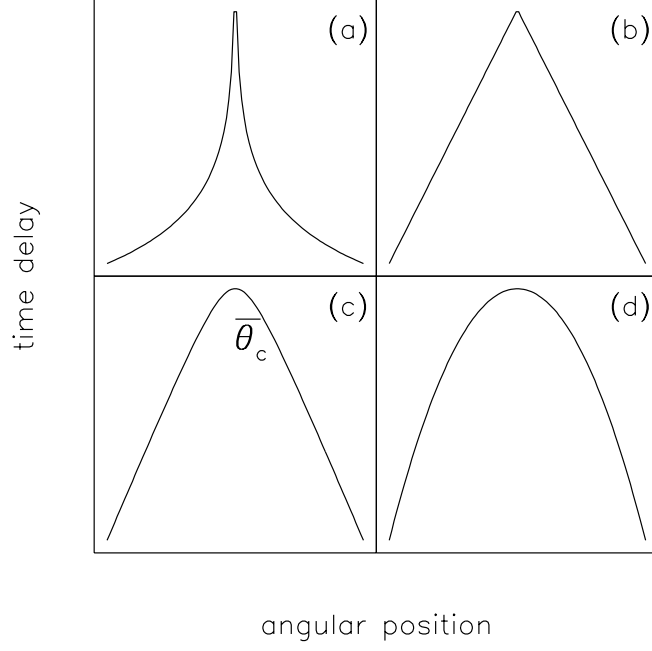


Figure 16: Gravitational time-delay functions for the four circularly symmetric effective potentials listed in Tab. 2. (a) point mass; (b) singular isothermal sphere; (c) softened isothermal sphere with core radius θ_c ; (d) constant density sheet.

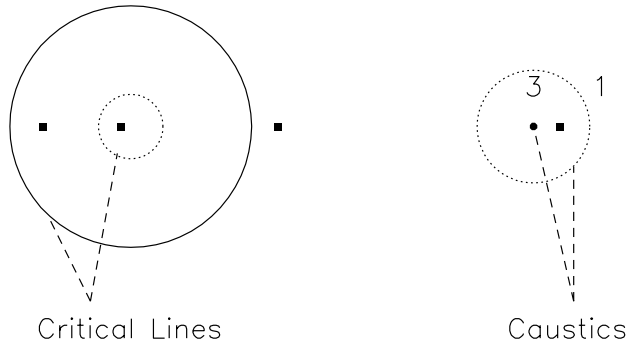


Figure 17: Imaging of a point source by a non-singular, circularly-symmetric lens. Left: image positions and critical lines; right: source position and corresponding caustics.

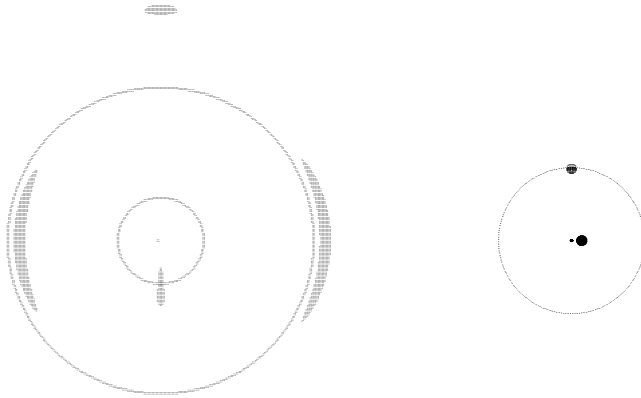


Figure 18: Imaging of an extended source by a non-singular circularly-symmetric lens. A source close to the point caustic at the lens center produces two tangentially oriented arc-like images close to the outer critical curve, and a faint image at the lens center. A source on the outer caustic produces a radially elongated image on the inner critical curve, and a tangentially oriented image outside the outer critical curve. Because of these image properties, the outer and inner critical curves are called *tangential* and *radial*, respectively.

caustic. Because of these image properties, the outer critical curve is called *tangential*, and the inner critical curve is called *radial*.

3.5 Non-Circularly-Symmetric Lens Models

A circularly symmetric lens model is much too idealized and is unlikely to describe real galaxies. Therefore, considerable work has gone into developing non-circularly symmetric models. The breaking of the symmetry leads to qualitatively new image configurations (see Grossman & Narayan 1988; Narayan & Grossman 1989; Blandford et al. 1989).

3.5.1 Elliptical Galaxy Model

To describe an elliptical galaxy lens, we should ideally consider elliptical isodensity contours. A straightforward generalization of the isothermal sphere with finite core gives

$$\Sigma(\theta_1, \theta_2) = \frac{\Sigma_0}{[\theta_c^2 + (1 - \epsilon)\theta_1^2 + (1 + \epsilon)\theta_2^2]^{1/2}}, \quad (64)$$

where θ_1, θ_2 are orthogonal coordinates along the major and minor axis of the lens measured from the center. The potential $\psi(\theta_1, \theta_2)$ corresponding to this density distribution has been calculated by Kassiola & Kovner (1993) but is somewhat complicated. For the specific case when the core

radius θ_c vanishes, the deflection angle and the magnification take on a simple form,

$$\begin{aligned}\alpha_1 &= \frac{8\pi G\Sigma_0}{\sqrt{2\epsilon}c^2} \tan^{-1} \left[\frac{\sqrt{2\epsilon} \cos \phi}{(1 - \epsilon \cos 2\phi)^{1/2}} \right], \\ \alpha_2 &= \frac{8\pi G\Sigma_0}{\sqrt{2\epsilon}c^2} \tanh^{-1} \left[\frac{\sqrt{2\epsilon} \sin \phi}{(1 - \epsilon \cos 2\phi)^{1/2}} \right], \\ \mu^{-1} &= 1 - \frac{8\pi G\Sigma_0}{c^2(\theta_1^2 + \theta_2^2)^{1/2}(1 - \epsilon \cos 2\phi)^{1/2}},\end{aligned}\tag{65}$$

where ϕ is the polar angle corresponding to the vector position $\vec{\theta} \equiv (\theta_1, \theta_2)$.

Instead of the elliptical density model, it is simpler and often sufficient to model a galaxy by means of an elliptical effective lensing potential (Blandford & Kochanek 1987)

$$\psi(\theta_1, \theta_2) = \frac{D_{\text{ds}}}{D_s} 4\pi \frac{\sigma_v^2}{c^2} [\theta_c^2 + (1 - \epsilon)\theta_1^2 + (1 + \epsilon)\theta_2^2]^{1/2},\tag{66}$$

where ϵ measures the ellipticity. The deflection law and magnification tensor corresponding to this potential are easily calculated using the equations given in Sect. 3.2. When ϵ is large, the elliptical potential model is inaccurate because it gives rise to dumbbell-shaped isodensity contours, but for small ϵ , it is a perfectly viable lens model.

3.5.2 External Shear

The environment of a galaxy, including any cluster surrounding the primary lens, will in general contribute both convergence and shear. The effective potential due to the local environment then reads

$$\psi(\theta_1, \theta_2) = \frac{\kappa}{2} (\theta_1^2 + \theta_2^2) + \frac{\gamma}{2} (\theta_1^2 - \theta_2^2)\tag{67}$$

in the principal axes system of the external shear, where the convergence κ and shear γ are locally independent of $\vec{\theta}$. An external shear breaks the circular symmetry of a lens and therefore it often has the same effect as introducing ellipticity in the lens (Kovner 1987). It is frequently possible to model the same system either with an elliptical potential or with a circular potential plus an external shear.

3.5.3 Image Configurations with a Non-Circularly Symmetric Lens

In contrast to the circularly symmetric case, for a non-circular lens the source, lens and images are not restricted to lie on a line. Therefore, it is not possible to analyze the problem via sections of the time delay surface as we did in Figs. 14 and 15. Fermat's principle and the time delay function are still very useful but it is necessary to visualize the full two-dimensional surface $t(\vec{\theta})$. Those who attended the lectures in Jerusalem may recall the lecturer demonstrating many of the qualitative features of imaging by elliptical lenses using a Mexican hat to simulate the time delay surface. In the following, we merely state the results.

Figures 19 and 20 illustrate the wide variety of image configurations produced by an elliptical galaxy lens (or a circularly symmetric lens with external shear). In each panel, the source plane with caustics is shown on the right, and the image configurations together with the critical curves are shown on the left. Compared to the circularly symmetric case, the first notable difference introduced by ellipticity is that the central caustic which was point-like is now expanded into a diamond shape and referred to as the *astroid* caustic. Figure 19 shows the images of a compact source moving away from the lens center along a symmetry line (right panel) and a line bisecting the two symmetry directions (left panel). A source behind the center of the lens has five images because it is enclosed by two caustics. One image appears at the lens center, and the four others form a cross-shaped pattern. When the source is moved outward, two of the four outer images move towards each other, merge, and disappear as the source approaches and then crosses the

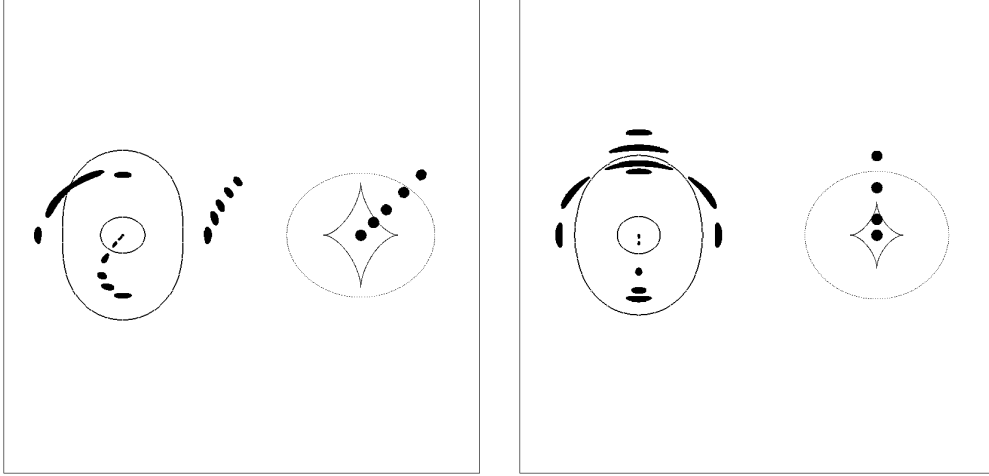


Figure 19: Compact source moving away from the center of an elliptical lens. Left panel: source crossing a fold caustic; right panel: source crossing a cusp caustic. In each panel, the diagram on the left shows critical lines and image positions and the diagram on the right shows caustics and source positions.

astroid (or tangential) caustic. Three images remain until the source crosses the radial caustic, when two more images merge and disappear at the radial critical curve. A single weakly distorted image is finally left when the source has crossed the outer caustic. When the source moves toward a cusp point (right panel of Fig. 19), three images merge to form a single image. All the image configurations shown in Fig. 19 are exhibited by various observed cases of lensing of QSOs and radio quasars (e.g. Keeton & Kochanek 1996).

Figure 20 illustrates what happens when a source with a larger angular size is imaged by the same lens model as in Fig. 19. Large arc-like images form which consist either of three or two merging images, depending on whether the source lies on top of a cusp in the tangential caustic (top left panel) or on an inter-cusp segment (a so-called fold caustic, top right panel). If the source is even larger (bottom panels), four images can merge, giving rise to complete or incomplete rings. Radio rings such as MG 1131+0456 (Hewitt et al. 1987) correspond to the configuration shown at bottom right in Fig. 20.

3.6 Studies of Galaxy Lensing

3.6.1 Detailed Models of Individual Cases of Lensing

Gravitational lens observations provide a number of constraints which can be used to model the mass distribution of the lens. The angular separation between the images determines the Einstein radius of the lens and therefore gives the mass M (eq. 22) or the velocity dispersion σ_v (eq. 44) in simple models. The appearance or absence of the central image constrains on the core size of the lens. The number of images and their positions relative to the lens determine the ellipticity of the galaxy, or equivalently the magnitude and orientation of an external shear. Since the radial and tangential magnifications of images reflect the local curvatures of the time-delay surface in

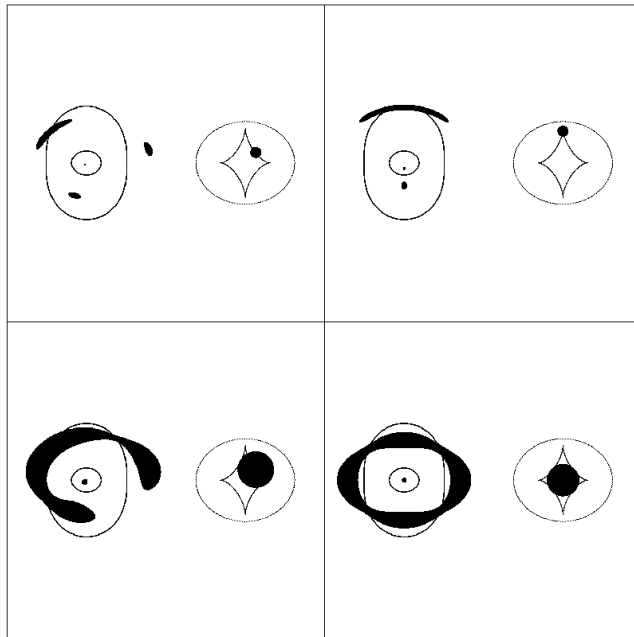


Figure 20: Images of resolved sources produced by an elliptical lens. Top panels: Large arcs consisting of two or three merging images are formed when the source lies on top of a fold section (top left panel) or a cusp point (top right panel) of the tangential caustic. Bottom panels: A source which covers most of the diamond-shaped caustic produces a ring-like image consisting of four merging images.

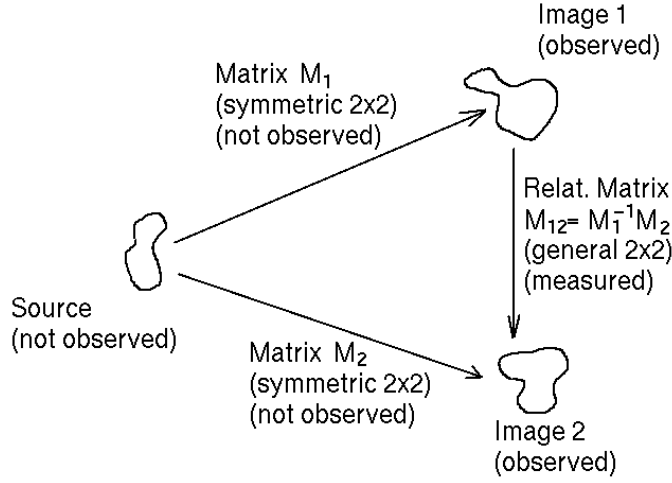


Figure 21: Shows an extended source which is mapped into two resolved images. While the source and the individual magnification matrices \mathcal{M}_1 and \mathcal{M}_2 are not observable, the relative magnification matrix $\mathcal{M}_{12} = \mathcal{M}_1^{-1} \mathcal{M}_2$ can be measured. This matrix provides four independent constraints on the lens model.

the corresponding directions, the relative image sizes constrain the slope of the density profile of the lens. This does not work very well if all one has are multiply imaged point images (Kochanek 1991). However, if the images have radio structure which can be resolved with VLBI, matters improve considerably.

Figure 21 shows an extended, irregularly shaped source which is mapped into two images which are each linear transformations of the unobservable source. The two transformations are described by symmetric 2×2 magnification matrices \mathcal{M}_1 and \mathcal{M}_2 (cf. eq. 52). These matrices cannot be determined from observations since the original source is not seen. However, the two images are related to each other by a linear transformation described by the relative magnification matrix $\mathcal{M}_{12} = \mathcal{M}_1^{-1} \mathcal{M}_2$ which can be measured via VLBI observations (Gorenstein et al. 1988; Falco, Gorenstein, & Shapiro 1991). The matrix \mathcal{M}_{12} is in general not symmetric and thus contains four independent components, which are each functions of the parameters of the lens model. In favorable cases, as in QSO 0957+561, it is even possible to measure the spatial gradient of \mathcal{M}_{12} (Garrett et al. 1994) which provides additional constraints on the model.

Radio rings with hundreds of independent pixels are particularly good for constraining the lens model. As shown in the bottom panels of Fig. 20, ring-shaped images are formed from extended sources which cover a large fraction of the central diamond-shaped caustic. Rings provide large numbers of independent observational constraints and are, in principle, capable of providing the most accurate mass reconstructions of the lens. However, special techniques are needed for analyzing rings. Three such techniques have been developed and applied to radio rings, viz.

- 1 The Ring Cycle algorithm (Kochanek et al. 1989) makes use of the fact that lensing conserves surface brightness. Surface elements of an extended image which arise from the same source element should therefore share the same surface brightness (to within observational errors). This provides a large number of constraints which can be used to reconstruct the shape of the original source and at the same time optimize a parameterized lens model.
- 2 The LensClean technique (Kochanek & Narayan 1992) is a generalization of the Ring Cycle algorithm which uses the Clean algorithm to allow for the finite beam of the radio telescope.
- 3 LensMEM (Wallington, Narayan, & Kochanek 1994; Wallington, Kochanek, & Narayan

1996) is analogous to LensClean, but uses the Maximum Entropy Method instead of Clean.

3.6.2 Statistical Modeling of Lens Populations

The statistics of lensed QSOs can be used to infer statistical properties of the lens population. In this approach, parameterized models of the galaxy and QSO populations in the universe are used to predict the number of lensed QSOs expected to be observed in a given QSO sample and to model the distributions of various observables such as the image separation, flux ratio, lens redshift, source redshift, etc. An important aspect of such studies is the detailed modeling of selection effects in QSO surveys (Kochanek 1993a) and proper allowance for magnification bias (Narayan & Wallington 1993). The lensing galaxies are usually modeled either as isothermal spheres or in terms of simple elliptical potentials, with an assumed galaxy luminosity function and a relation connecting luminosity and galaxy mass (or velocity dispersion). The QSO number-count as a function of redshift should be known since it strongly influences the lensing probability.

Statistical studies have been fairly successful in determining properties of the galaxy population in the universe, especially at moderate redshifts where direct observations are difficult. Useful results have been obtained on the number density, velocity dispersions, core radii, etc. of lenses. Resolved radio QSOs provide additional information on the internal structure of galaxy lenses such as their ellipticities (Kochanek 1996b). By and large, the lens population required to explain the statistics of multiply imaged optical and radio QSOs turns out to be consistent with the locally observed galaxy population extrapolated to higher redshifts (Kochanek 1993b; Maoz & Rix 1993; Surdej et al. 1993; see below).

3.7 Astrophysical Results from Galaxy Lensing

3.7.1 Galaxy Structure

The structure of galaxies influences lensing statistics as well as the appearances of individual lensed objects. Gravitational lensing can therefore be used to constrain galaxy models in various ways.

As described earlier, galaxy lens models predict a weak central image whose flux depends on the core radius of the galaxy. The central image is missing in virtually every known multiply-imaged quasar. The lensing galaxies in these cases must therefore have very small core radii, $r_c < 200$ pc (Wallington & Narayan 1993; Kassiola & Kovner 1993; Grogin & Narayan 1996).

Kochanek (1993b) has shown that the observed distribution of image separations in the observed lens sample of quasars requires that most galaxies must have dark halos with characteristic velocity dispersions of $\sigma_{\text{dark}}^* \sim 220 \pm 20$ km s⁻¹. If these dark halos were absent, virtually no image separations larger than 2'' would be produced (Maoz & Rix 1993), whereas several wide separation examples are known. Multiply-imaged quasars do not generally constrain the size of the halo because the constraints only extend out to about the Einstein radius, which is ~ 10 kpc at the distance of the lens. The largest halo inferred from direct modeling of a multiply-imaged quasar is in the lensing galaxy of QSO 0957+561; the halo of this galaxy has been shown to have a radius of at least $15h^{-1}$ kpc, where $h = H_0/100$ km s⁻¹ Mpc⁻¹ is the reduced Hubble constant (Grogin & Narayan 1996). Brainerd et al. (1996) investigated weak lensing of background galaxies by foreground galaxies and found statistical evidence for halos extending out to radii ~ 100 kpc. At these radii, they determined that an L_* galaxy must have a mass $\sim 10^{12} M_\odot$.

Only in two cases has it been possible to constrain significantly the radial mass density variation of the lensing galaxy. Assuming a surface mass density profile $\Sigma \propto r^{-\alpha}$, the best fitting values of α in these two examples are

$$\alpha = \begin{cases} (0.9 - 1.1) & \text{in MG 1654+134} & (\text{Kochanek 1995a}) \\ (1.0 - 1.2) & \text{in QSO 0957+561} & (\text{Grogin \& Narayan 1996}) \end{cases} \quad (68)$$

Both sources have particularly good data — the first is a radio ring and the second has extensive VLBI observations — and it is this feature that allows a good constraint on α . Note that the density variation is close to isothermal in both cases.

The observed morphologies of images in lensed quasars are similar to those shown in Fig. 19, which means that most lenses are not circularly symmetric. If the non-circularity is entirely due to the ellipticity of the galaxy mass, then typical ellipticities are fairly large, $\sim E3 - E4$ (Kochanek 1996b). However, it is possible that part of the effect comes from external shear. The data are currently not able to distinguish very well between the effects of galaxy ellipticity and external shear. In many well-modeled examples, the mass ellipticity required to fit the images is larger than the ellipticity of the galaxy isophotes, suggesting either that the dark matter is more asymmetric than the luminous matter or that there is a significant contribution from external shear (Kochanek 1996b; Bar-Kana 1996).

3.7.2 Galaxy Formation and Evolution

The angular separations of multiple images depend on the lens mass, and the number of observed multiply imaged quasars with a given separation depends on the number density of galaxies with the corresponding mass. The usual procedure to set limits on the galaxy population starts with the present galaxy population and extrapolates it to higher redshifts assuming some parameterized prescription of evolution. The parameters are then constrained by comparing the observed statistics of lensed sources to that predicted by the model (Kochanek 1993b; Maoz & Rix 1993; Rix et al. 1994; Mao & Kochanek 1994).

If galaxies formed recently, most of the optical depth for multiple imaging will be from low-redshift galaxies. An analysis which uses all the known information on lensed quasars, such as the redshifts of lenses and sources, the observed fraction of lensed quasars, and the distribution of image separations, can be used to set limits on how recently galaxies could have formed. Mao & Kochanek (1994) conclude that most galaxies must have collapsed and formed by $z \sim 0.8$ if the universe is well described by the Einstein-de Sitter model.

If elliptical galaxies are assembled from merging spiral galaxies, then with increasing redshift the present population of ellipticals is gradually replaced by spirals. This does not affect the probability of producing lensed quasars as the increase in the number of lens galaxies at high redshift is compensated by the reduced lensing cross-sections of these galaxies. However, because of their lower velocity dispersion, spirals produce smaller image separations than ellipticals (the image splitting is proportional to σ_v^2 , cf. eq. 44). Therefore, a merger scenario will predict smaller image separations in high redshift quasars, and the observed image separations can be used to constrain the merger rate (Rix et al. 1994). Assuming that the mass of the galaxies scales with σ_v^4 and is conserved in mergers, Mao & Kochanek (1994) find that no significant mergers could have occurred more recently than $z \sim 0.4$ in an Einstein-de Sitter universe.

If the cosmological constant is large, say $\Lambda > 0.6$, the volume per unit redshift is much larger than in an Einstein-de Sitter universe. For a fixed number density of galaxies, the total number of available lenses then increases steeply. For such model universes, lens statistics would be consistent with recent rapid evolution of the galaxy population. However, studies of gravitational clustering and structure formation show that galaxies form at high redshifts precisely when Λ is large. When this additional constraint is included it is found that there is no scenario which allows recent galaxy formation or evolution in the universe (see also Sect. 3.7.5).

Since lensing statistics are fully consistent with the known local galaxy population extrapolated to redshifts $z \sim 1$, the number densities of any dark “failed” galaxies are constrained quite strongly. As a function of velocity dispersion σ_* , the current constraints are (Mao & Kochanek 1994)

$$n_{\text{dark}} < \begin{cases} 0.15 h^3 \text{Mpc}^{-3} & \text{for } \sigma_* = 100 \text{ km s}^{-1} \\ 0.032 h^3 \text{Mpc}^{-3} & \text{for } \sigma_* = 150 \text{ km s}^{-1} \\ 0.017 h^3 \text{Mpc}^{-3} & \text{for } \sigma_* = 200 \text{ km s}^{-1} \end{cases} . \quad (69)$$

3.7.3 Constraint on CDM

The popular cold dark matter (CDM) scenario of structure formation in its “standard” variant ($\Omega_0 = 1$, $\Lambda_0 = 0$ and COBE normalized) predicts the formation of large numbers of dark matter

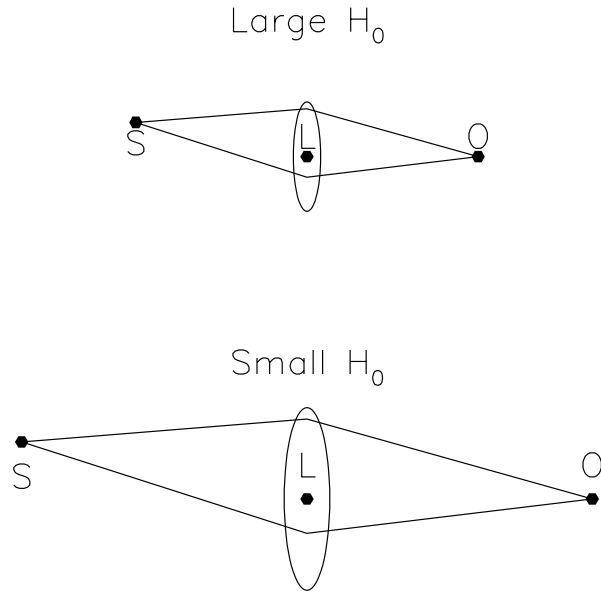


Figure 22: Sketch of the dependence of the overall scale of a lens system on the value of the Hubble constant.

halos in the mass range between galaxies and galaxy clusters. The implications of these halos for lensing were considered by Narayan & White (1988) and more recently by Cen et al. (1994), Wambsganss et al. (1995) and Kochanek (1995b). The latter authors have shown quite convincingly that the standard CDM model produces many more wide-separation quasar pairs than observed. To save CDM, either the normalization of the model needs to be reduced to $\sigma_8 \sim 0.5 \pm 0.2$, or the long-wavelength slope of the power spectrum needs to be lowered to $n \sim 0.5 \pm 0.2$. Both of these options are inconsistent with the COBE results. The problem of the over-production of wide angle pairs is just a manifestation of the well-known problem that standard COBE-normalized CDM over-produces cluster-scale mass condensations by a large factor. Models which are adjusted to fit the observed number density of clusters also satisfy the gravitational lens constraint.

If the dark halos have large core radii, their central density could drop below the critical value for lensing and this would reduce the predicted number of wide-separation lens systems. Large core radii thus may save standard CDM (Flores & Primack 1996), but there is some danger of fine-tuning in such an explanation. As discussed in Sect. 3.7.1, galaxy cores are quite small. Therefore, one needs to invoke a rather abrupt increase of core radius with increasing halo mass.

3.7.4 Hubble Constant

The lens equation is dimensionless, and the positions of images as well as their magnifications are dimensionless numbers. Therefore, information on the image configuration alone does not provide any constraint on the overall scale of the lens geometry or the value of the Hubble constant. Refsdal (1964) realized that the time delay, however, is proportional to the absolute scale of the system and does depend on H_0 (cf. Fig. 22).

To see this, we first note that the geometrical time delay is simply proportional to the path lengths of the rays which scale as H_0^{-1} . The potential time delay also scales as H_0^{-1} because the linear size of the lens and its mass have this scaling. Therefore, for any gravitational lens system,

the quantity

$$H_0 \Delta\tau \quad (70)$$

depends only on the lens model and the geometry of the system. A good lens model which reproduces the positions and magnifications of the images provides the scaled time delay $H_0 \Delta\tau$ between the images. Therefore, a measurement of the time delay $\Delta\tau$ will yield the Hubble constant H_0 (Refsdal 1964, 1966a).

To measure the time delay, the fluxes of the images need to be monitored over a period of time significantly longer than the time delay in order to achieve reasonable accuracy. In fact, the analysis of the resulting light curves is not straightforward because of uneven data sampling, and careful and sophisticated data analysis techniques have to be applied. QSO 0957+561 has been monitored both in the optical (Vanderriest et al. 1989; Schild & Thomson 1993) and radio wavebands (Lehár et al. 1992). Unfortunately, analysis of the data has led to two claimed time delays:

$$\Delta\tau = (1.48 \pm 0.03) \text{ years} \quad (71)$$

(Press, Rybicki, & Hewitt 1992a,b) and

$$\Delta\tau \simeq 1.14 \text{ years} \quad (72)$$

(Schild & Thomson 1993; Pelt et al. 1994, 1996). The discrepancy appears to have been resolved in favor of the shorter delay (Sky & Telescope, June 1996, p10).

In addition to a measurement of the time delay, it is also necessary to develop a reliable model to calculate the value of $H_0 \Delta\tau$. QSO 0957+561 has been studied by a number of groups over the years, with recent work incorporating constraints from VLBI imaging (Falco et al. 1991). Grogin & Narayan (1996) estimate the Hubble constant to be given by

$$H_0 = (82 \pm 6) (1 - \kappa) \left(\frac{\Delta\tau}{1.14 \text{ yr}} \right)^{-1} \text{ km s}^{-1} \text{ Mpc}^{-1} \quad (73)$$

where κ refers to the unknown convergence due to the cluster surrounding the lensing galaxy. Since κ due to the cluster cannot be negative, this result directly gives an upper bound on the Hubble constant ($H_0 < 88 \text{ km s}^{-1} \text{ Mpc}^{-1}$ for $\Delta\tau = 1.14$ years). Actually, κ can also be modified by large scale structure along the line of sight. In contrast to the effect of the cluster, this fluctuation can have either sign, but the rms amplitude is estimated to be only a few per cent (Seljak 1994; Bar-Kana 1996).

To obtain an actual value of H_0 instead of just an upper bound, we need an independent estimate of κ . Studies of the cluster suggest that $0.1 < \kappa < 0.2$ but this is very approximate. A better alternative is to measure the velocity dispersion of the lensing galaxy from which it is possible to estimate κ (Falco et al. 1992; Grogin & Narayan 1996). Although most models of QSO 0957+561 are based on a spherically symmetric galaxy embedded in an external shear (mostly due to the cluster), introduction of ellipticity in the galaxy, or a point mass at the galaxy core, or substructure in the cluster seem to have little effect on the estimate of H_0 (Grogin & Narayan 1996).

A measurement of the time delay has also been attempted in the Einstein ring system B 0218+357. In this case, a single galaxy is responsible for the small image splitting of $0.3''$. The time delay has been determined to 12 ± 3 days (1σ confidence limit) which translates to $H_0 \sim 60 \text{ km s}^{-1} \text{ Mpc}^{-1}$ (Corbett et al. 1996).

The determination of H_0 through gravitational lensing has a number of advantages over other techniques.

- 1 The method works directly with sources at large redshifts, $z \sim 0.5$, whereas most other methods are local (observations within $\sim 100 \text{ Mpc}$) where peculiar velocities are still comparable to the Hubble flow.

Figure 23: *Hubble Space Telescope* image of the cluster Abell 2218, showing a number of arcs and arclets around the two centers of the cluster. (NASA HST Archive)

- 2 While other determinations of the Hubble constant rely on distance ladders which progressively reach out to increasing distances, the measurement via gravitational time delay is a one-shot procedure. One measures directly the geometrical scale of the lens system. This means that the lens-based method is absolutely independent of every other method and therefore provides a valuable test of other determinations.
- 3 The lens-based method is based on fundamental physics (the theory of light propagation in General Relativity), which is fully tested in the relevant weak-field limit of gravity. Other methods rely on models for variable stars (Cepheids) or supernova explosions (Type II), or empirical calibrations of standard candles (Tully-Fisher distances, Type I supernovae). The lensing method does require some information on the “shapes” of galaxies which is used to guide the choice of a parameterized lens model.

3.7.5 Cosmological Constant

A large cosmological constant Λ_0 increases the volume per unit redshift of the universe at high redshift. As Turner (1990) realized, this means that the relative number of lensed sources for a fixed comoving number density of galaxies increases rapidly with increasing Λ_0 . Turning this around it is possible to use the observed probability of lensing to constrain Λ_0 . This method has been applied by various authors (Turner 1990; Fukugita & Turner 1991; Fukugita et al. 1992; Maoz & Rix 1993; Kochanek 1996a), and the current limit is $\Lambda_0 < 0.65$ (2σ confidence limit) for a universe with $\Omega_0 + \Lambda_0 = 1$.

A completely independent approach (Kochanek 1992) considers the redshift distribution of lenses. For a given source redshift, the probability distribution of z_d peaks at higher redshift with increasing Λ_0 . Once again, by comparing the observations against the predicted distributions one obtains an upper limit on Λ_0 . This method is less sensitive than the first, but gives consistent results.

4 Lensing by Galaxy Clusters and Large-Scale Structure

Two distinct types of lensing phenomena are observed with clusters of galaxies (Fig. 23):

- 1 Rich centrally condensed clusters occasionally produce giant arcs when a background galaxy happens to be aligned with one of the cluster caustics. These instances of lensing are usually analyzed with techniques similar to those described in Sect. 2 for galaxy lenses. In brief, a parameterized lens model is optimized so as to obtain a good fit to the observed image.
- 2 Every cluster produces weakly distorted images of large numbers of background galaxies. These images are called arclets and the phenomenon is referred to as weak lensing. With the development of the Kaiser & Squires (1993) algorithm and its variants, weak lensing is being used increasingly to derive parameter-free two-dimensional mass maps of lensing clusters.

In addition to these two topics, we also discuss in this section weak lensing by large-scale structure in the universe. This topic promises to develop into an important branch of gravitational lensing, and could in principle provide a direct measurement of the primordial power spectrum $P(k)$ of the density fluctuations in the universe.

4.1 Strong Lensing by Clusters — Giant Arcs

4.1.1 Basic Optics

We begin by summarizing a few features of generic lenses which we have already discussed in the previous sections. A lens is fully characterized by its surface mass density $\Sigma(\theta)$. Strong lensing, which is accompanied by multiple imaging, requires that the surface mass density somewhere in the lens should be larger than the critical surface mass density,

$$\Sigma \gtrsim \Sigma_{\text{cr}} = 0.35 \text{ g cm}^{-3} \left(\frac{D}{\text{Gpc}} \right)^{-1}, \quad (74)$$

where D is the effective lensing distance defined in eq. (18). A lens which satisfies this condition produces one or more caustics. Examples of the caustics produced by an elliptical lens with a finite core are shown in Fig. 19. Sources outside all caustics produce a single image; the number of images increases by two upon each caustic crossing towards the lens center. As illustrated in Figs. 19 and 20, extended sources like galaxies produce large arcs if they lie on top of caustics. The largest arcs are formed from sources on cusp points, because then three images of a source merge to form the arc (cf. the right panel in Fig. 19 or the top right panel in Fig. 20). At the so-called “lips” and “beak-to-beak” caustics, which are related to cusps, similarly large arcs are formed. Sources on a fold caustic give rise to two rather than three merging images and thus form moderate arcs.

4.1.2 Cluster Mass Inside a Giant Arc

The location of an arc in a cluster provides a simple way to estimate the projected cluster mass within a circle traced by the arc (cf. Fig. 24). For a circularly symmetric lens, the average surface mass density $\langle \Sigma \rangle$ within the tangential critical curve equals the critical surface mass density Σ_{cr} . Tangentially oriented large arcs occur approximately at the tangential critical curves. The radius θ_{arc} of the circle traced by the arc therefore gives an estimate of the Einstein radius θ_{E} of the cluster.

Thus we have

$$\langle \Sigma(\theta_{\text{arc}}) \rangle \approx \langle \Sigma(\theta_{\text{E}}) \rangle = \Sigma_{\text{cr}}, \quad (75)$$

and we obtain for the mass enclosed by $\theta = \theta_{\text{arc}}$

$$M(\theta) = \Sigma_{\text{cr}} \pi (D_{\text{d}} \theta)^2 \approx 1.1 \times 10^{14} M_{\odot} \left(\frac{\theta}{30''} \right)^2 \left(\frac{D}{1 \text{ Gpc}} \right). \quad (76)$$

Assuming an isothermal model for the mass distribution in the cluster and using eq. (44), we obtain an estimate for the velocity dispersion of the cluster,

$$\sigma_v \approx 10^3 \text{ km s}^{-1} \left(\frac{\theta}{28''} \right)^{1/2} \left(\frac{D_{\text{s}}}{D_{\text{ds}}} \right)^{1/2}. \quad (77)$$

In addition to the lensing technique, two other methods are available to obtain the mass of a cluster: the observed velocity dispersion of the cluster galaxies can be combined with the virial theorem to obtain one estimate, and observations of the X-ray gas combined with the condition of hydrostatic equilibrium provides another. These three quite independent techniques yield masses which agree with one another to within a factor $\sim 2 - 3$.

The mass estimate (76) is based on very simple assumptions. It can be improved by modeling the arcs with parameterized lens mass distributions and carrying out more detailed fits of the observed arcs. We list in Tab. 3 masses, mass-to-blue-light ratios, and velocity dispersions of three clusters with prominent arcs. Additional results can be found in the review article by Fort & Mellier (1994).

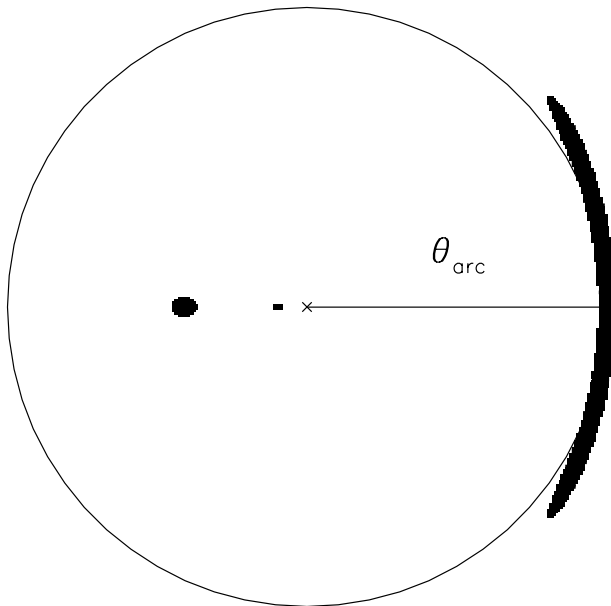


Figure 24: Tangential arcs constrain the cluster mass within a circle traced by the arcs.

Table 3: Masses, mass-to-blue-light ratios, and velocity dispersions for three clusters with prominent arcs.

Cluster	M (M_{\odot})	M/L_B (solar)	σ km s $^{-1}$	Reference
A 370	$\sim 10^{14}$	~ 200	~ 1350	Grossman & Narayan 1989 Bergmann et al. 1990 Kneib et al. 1993
A 2390	$\sim 1.5 \times 10^{14}$	~ 120	~ 1250	Pelló et al. 1991
MS 2137–23	$\sim 5 \times 10^{13}$	~ 250	~ 1100	Mellier et al. 1993

Table 4: Limits on cluster core radii from models of large arcs.

Cluster	r_{core} (kpc)	Reference
A 370	< 60	Grossman & Narayan (1989)
	< 100	Kneib et al. (1993)
MS 2137–23	~ 50	Mellier et al. (1993)
Cl 0024+1654	< 130	Bonnet et al. (1994)
MS 0440+0204	$\ll 90$	Luppino et al. (1993)

4.1.3 Asphericity of Cluster Mass

The fact that the observed giant arcs never have counter-arcs of comparable brightness, and rarely have even small counter-arcs, implies that the lensing geometry has to be non-spherical (Grossman & Narayan 1988; Kovner 1989; see also Figs. 19 and 20). Cluster potentials therefore must have substantial quadrupole and perhaps also higher multipole moments. In the case of A 370, for example, there are two cD galaxies, and the potential quadrupole estimated from their separation is consistent with the quadrupole required to model the observed giant arc (Grossman & Narayan 1989). The more detailed model of A 370 by Kneib et al. (1993) shows a remarkable agreement between the lensing potential and the strongly aspheric X-ray emission of the cluster.

Large deviations of the lensing potentials from spherical symmetry also help increase the probability of producing large arcs. Bergmann & Petrosian (1993) argued that the apparent abundance of large arcs relative to small arcs and arclets can be reconciled with theoretical expectations if aspheric lens models are taken into account. Bartelmann & Weiss (1994) and Bartelmann, Steinmetz, & Weiss (1995) showed that the probability for large arcs can be increased by more than an order of magnitude if aspheric cluster models with significant substructure are used instead of smooth spherically symmetric models. The essential reason for this is that the largest (three-image) arcs are produced by cusp caustics, and asymmetry increases the number of cusps on the cluster caustics.

4.1.4 Core Radii

If a cluster is able to produce large arcs, its surface-mass density in the core must be approximately supercritical, $\Sigma \gtrsim \Sigma_{\text{cr}}$. If applied to simple lens models, e.g. softened isothermal spheres, this condition requires

$$\theta_{\text{core}} \lesssim 15'' \left(\frac{\sigma_v}{10^3 \text{ km s}^{-1}} \right)^2 \left(\frac{D_{\text{ds}}}{D_s} \right). \quad (78)$$

Narayan, Blandford, & Nityananda (1984) argued that cluster mass distributions need to have smaller core radii than those derived from optical and X-ray observations if they are to produce strong gravitational lens effects. This has been confirmed by many later efforts to model giant arcs. In virtually every case the core radius estimated from lensing is significantly smaller than the estimates from optical and X-ray data. Some representative results on lens-derived core radii are listed in Tab. 4, where the estimates correspond to $H_0 = 50 \text{ km s}^{-1} \text{ Mpc}^{-1}$.

Statistical analyses based on spherically symmetric cluster models lead to similar conclusions. Miralda-Escudé (1992, 1993) argued that cluster core radii can hardly be larger than the curvature radii of large arcs. Wu & Hammer (1993) claimed that clusters either have to have singular cores or density profiles much steeper than isothermal in order to reproduce the abundance of large arcs. Although this conclusion can substantially be altered once deviations from spherical symmetry are taken into account (Bartelmann et al. 1995), it remains true that we require $r_{\text{core}} \lesssim 100 \text{ kpc}$ in all observed clusters. Cores of this size can also be reconciled with large-arc statistics.

Interestingly, there are at least two observations which seem to indicate that cluster cores, although small, must be finite. Fort et al. (1992) discovered a radial arc near the center of MS 2137–23, and Smail et al. (1995b) found a radial arc in A 370. To produce a radial arc with a softened isothermal sphere model, the core radius has to be roughly equal to the distance between the cluster center and the radial arc (cf. Fig. 19). Mellier, Fort, & Kneib (1993) find $r_{\text{core}} \gtrsim 40$ kpc in MS 2137–23, and Smail et al. (1995b) infer $r_{\text{core}} \sim 50$ kpc in A 370. Bergmann & Petrosian (1993) presented a statistical argument in favor of finite cores by showing that lens models with singular cores produce fewer large arcs (relative to small arcs) than observed. The relative abundance increases with a small finite core. These results, however, have to be interpreted with caution because it may well be that the softened isothermal sphere model is inadequate to describe the interiors of galaxy clusters. While this particular model indeed requires core radii on the order of the radial critical radius, other lens models can produce radial arcs without having a flat core, and there are even singular density profiles which can explain radial arcs (Miralda-Escudé 1995; Bartelmann 1996). Such singular profiles for the dark matter are consistent with the fairly large core radii inferred from the X-ray emission of clusters, if the intracluster gas is isothermal and in hydrostatic equilibrium with the dark-matter potential (Navarro, Frenk, & White 1996; J.P. Ostriker, private communication).

4.1.5 Radial Density Profile

Many of the observed giant arcs are unresolved in the radial direction, some of them even when observed under excellent seeing conditions or with the *Hubble Space Telescope*. Since the faint blue background galaxies which provide the source population for the arcs seem to be resolved (e.g. Tyson 1995), the giant arcs appear to be demagnified in width. It was realized by Hammer & Rigaut (1989) that spherically symmetric lenses can radially demagnify giant arcs only if their radial density profiles are steeper than isothermal. The maximum demagnification is obtained for a point mass lens, where it is a factor of two. Kovner (1989) and Hammer (1991) demonstrated that, irrespective of the mass profile and the symmetry of the lens, the thin dimension of an arc is compressed by a factor $\approx 2(1 - \kappa)$, where κ is the convergence at the position of the arc. Arcs which are thinner than the original source therefore require $\kappa \lesssim 0.5$. Since giant arcs have to be located close to those critical curves in the lens plane along which $1 - \kappa - \gamma = 0$, large and thin arcs additionally require $\gamma \gtrsim 0.5$.

In principle, the radius of curvature of large arcs relative to their distance from the cluster center can be used to constrain the steepness of the radial density profile (Miralda-Escudé 1992, 1993), but results obtained from observed arcs are not yet conclusive (Grossman & Saha 1994). One problem with this method is that substructure in clusters tends to enlarge curvature radii irrespective of the mass profile of the dominant component of the cluster (Miralda-Escudé 1993; Bartelmann et al. 1995).

Wu & Hammer (1993) argued for steep mass profiles on statistical grounds because the observed abundance of large arcs appears to require highly centrally condensed cluster mass profiles in order to increase the central mass density of clusters while keeping their total mass constant. However, their conclusions are based on spherically symmetric lens models and are significantly changed when the symmetry assumption is dropped (Bartelmann et al. 1995).

It should also be kept in mind that not all arcs are thin. Some “thick” and resolved arcs are known (e.g. in A 2218, Pelló-Descayre et al. 1988; and in A 2390, Pelló et al. 1991), and it is quite possible that thin arcs predominate just because they are more easily detected than thick ones due to observational selection effects. Also, Miralda-Escudé (1992, 1993) has argued that intrinsic source ellipticity can increase the probability of producing thin arcs, while Bartelmann et al. (1995) showed that the condition $\kappa \lesssim 0.5$ which is required for thin arcs can be more frequently fulfilled in clusters with substructure where the shear is larger than in spherically symmetric clusters.

4.1.6 Mass Sub-Condensations

The cluster A 370 has two cD galaxies and is a clear example of a cluster with multiple mass centers. A two-component mass model centered on the cD galaxies (Kneib et al. 1993) fits very well the lens data as well as X-ray and deep optical images of the cluster. Abell 2390 is an interesting example because it contains a “straight arc” (Pelló et al. 1991, see also Mathez et al. 1992) which can be produced only with either a lips or a beak-to-beak caustic (Kassiola, Kovner, & Blandford 1992). If the arc is modeled with a lips caustic, it requires the mass peak to be close to the location of the arc, but this is not where the cluster light is centered. With a beak-to-beak caustic, the model requires two separate mass condensations, one of which could be at the peak of the luminosity, but then the other has to be a dark condensation. Pierre et al. (1996) find enhanced X-ray emission at a plausible position of the secondary mass clump, and from a weak lensing analysis Squires et al. (1996b) find a mass map which is consistent with a mass condensation at the location of the enhanced X-ray emission.

Abell 370 and A 2390 are the most obvious examples of what is probably a widespread phenomenon, namely that clusters are in general not fully relaxed but have substructure as a result of ongoing evolution. If clusters are frequently clumpy, this can lead to systematic effects in the statistics of arcs and in the derived cluster parameters (Bartelmann et al. 1995; Bartelmann 1995b).

4.1.7 Lensing Results vs. Other Mass Determinations

Enclosed Mass Three different methods are currently used to estimate cluster masses. Galaxy velocity dispersions yield a mass estimate from the virial theorem, and hence the galaxies have to be in virial equilibrium for such estimates to be valid. It may also be that the velocities of cluster galaxies are biased relative to the velocities of the dark matter particles (Carlberg 1994), though current estimates suggest that the bias is no more than about 10%. The X-ray emission of rich galaxy clusters is dominated by free-free emission of thermal electrons and therefore depends on the squared density of the intracluster gas, which in turn traces the gravitational potential of the clusters. Such estimates usually assume that the cluster gas is in thermal hydrostatic equilibrium and that the potential is at least approximately spherically symmetric. Finally, large arcs in clusters provide a mass estimate through eq. (76) or by more detailed modeling. These three mass estimates are in qualitative agreement with each other up to factors of $\approx 2 - 3$.

Miralda-Escudé & Babul (1995) compared X-ray and large-arc mass estimates for the clusters A 1689, A 2163 and A 2218. They took into account deviations from spherical symmetry and obtained lensing masses from individual lens models which reproduce the observed arcs. They arrived at the conclusion that in A 1689 and A 2218 the mass required for producing the large arcs is higher by a factor of $2 - 2.5$ than the mass required for the X-ray emission, and proposed a variety of reasons for such a discrepancy, among them projection effects and non-thermal pressure support. Loeb & Mao (1994) specifically suggested that strong turbulence and magnetic fields in the intracluster gas may constitute a significant non-thermal pressure component in A 2218 and thus render the X-ray mass estimate too low. Bartelmann & Steinmetz (1996) used gas dynamical cluster simulations to compare their X-ray and lensing properties. They found a similar discrepancy as that identified by Miralda-Escudé & Babul (1995) in those clusters that show structure in the distribution of line-of-sight velocities of the cluster particles, indicative of merging or infall along the line-of-sight. The discrepancy is probably due to projection effects.

Bartelmann (1995b) showed that cluster mass estimates obtained from large arcs by straightforward application of eq. (76) are systematically too high by a factor of ≈ 1.6 on average, and by as much as a factor of ≈ 2 in 1 out of 5 cases. This discrepancy arises because eq. (76) assumes a smooth spherically symmetric mass distribution whereas realistic clusters are asymmetric and have substructure. Note that Daines et al. (1996) found evidence for two or more mass condensations along the line of sight towards A 1689, while the arclets in A 2218 show at least two mass concentrations. It appears that cluster mass estimates from lensing require detailed lens models in order to be accurate to better than $\approx 30 - 50$ per cent. In the case of MS 1224, Fahlman et al.

(1994) and Carlberg, Yee, & Ellingson (1994) have obtained masses using the Kaiser & Squires weak-lensing cluster reconstruction method. Their mass estimates are 2 – 3 times higher than the cluster’s virial mass. Carlberg et al. find evidence from velocity measurements that there is a second poor cluster in the foreground of MS 1224 which may explain the result. All of these mass discrepancies illustrate that cluster masses must still be considered uncertain to a factor of ≈ 2 in general.

Core Radii Lensing estimates of cluster core radii are generally much smaller than the core radii obtained from optical or X-ray data. The upper limits on the core radii from lensing are fairly robust and probably reliable. Many clusters with large arcs have cD galaxies which can steepen the central mass profile of the cluster. However, there are also non-cD clusters with giant arcs, e.g. A 1689 and Cl 1409 (Tyson 1990), and MS 0440+02 (Luppino et al. 1993). In fact, Tyson (1990) claims that these two clusters have cores smaller than $100 h^{-1}$ kpc, similar to upper limits for core radii found in other arc clusters with cD galaxies. As mentioned in Sect. 4.1.4, even the occurrence of radial arcs in clusters does not necessarily require a non-singular core, and so all the lensing data are consistent with singular cores in clusters. The X-ray core radii depend on whether or not the cooling regions of clusters are included in the emissivity profile fits, because the cooling radii are of the same order of magnitude as the core radii. If cooling is included, the best-fit core radii are reduced by a factor of $\simeq 4$ (Gerbal et al. 1992; Durret et al. 1994). Also, isothermal gas in hydrostatic equilibrium in a singular dark-matter distribution develops a flat core with a core radius similar to those observed. Therefore, the strongly peaked mass distributions required for lensing seem to be quite compatible with the extended X-ray cores observed.

Does Mass Follow Light? Leaving the core radius aside, does mass follow light? It is clear that the mass cannot be as concentrated within the galaxies as the optical light is (e.g. Bergmann, Petrosian, & Lynds 1990). However, if the optical light is smoothed and assumed to trace the mass, then the resulting mass distribution is probably not very different from the true mass distribution. For instance, in A 370, the elongation of the mass distribution required for the giant arc is along the line connecting the two cD galaxies in the cluster (Grossman & Narayan 1989) and in fact Kneib et al. (1993) are able to achieve an excellent fit of the giant arc and several arclets with two mass concentrations surrounding the two cDs. Their model potential also agrees very well with the X-ray emission of the cluster. In MS 2137, the optical halo is elongated in the direction indicated by the arcs for the overall mass asymmetry (Mellier et al. 1993), and in Cl 0024, the mass distribution is elongated in the same direction as the galaxy distribution (Warrington, Kochanek, & Koo 1995). Smail et al. (1995a) find that the mass maps of two clusters reconstructed from weak lensing agree fairly well with their X-ray emission. An important counterexample is the cluster A 2390, where the straight arc requires a mass concentration which is completely dark in the optical (Kassiola et al. 1992). Pierre et al. (1996), however, find excess X-ray emission at a position compatible with the arc.

What Kinds of Clusters Produce Giant Arcs? Which parameters determine whether or not a galaxy cluster is able to produce large arcs? Clearly, large velocity dispersions and small core radii favor the formation of arcs. As argued earlier, intrinsic asymmetries and substructure also increase the ability of clusters to produce arcs because they increase the shear and the number of cusps in the caustics.

The abundance of arcs in X-ray luminous clusters appears to be higher than in optically selected clusters. At least a quarter, maybe half, of the 38 X-ray bright clusters selected by Le Fèvre et al. (1994) contain large arcs, while Smail et al. (1991) found only one large arc in a sample of 19 distant optically selected clusters. However, some clusters which are prominent lenses (A 370, A 1689, A 2218) are moderate X-ray sources, while other clusters which are very luminous X-ray sources (A 2163, Cl 1455) are poor lenses. The correlation between X-ray brightness and enhanced occurrence of arcs may suggest that X-ray bright clusters are more massive and/or more centrally condensed than X-ray quiet clusters.

Substructure appears to be at least as important as X-ray brightness for producing giant arcs. For example, A 370, A 1689 and A 2218 all seem to have clumpy mass distributions. Bartelmann & Steinmetz (1996) used numerical cluster simulations to show that the optical depth for arc formation is dominated by clusters with intermediate rather than the highest X-ray luminosities.

Another possibility is that giant arcs preferentially form in clusters with cD galaxies. A 370, for instance, even has two cDs. However, non-cD clusters with giant arcs are known, e.g. A 1689, Cl 1409 (Tyson et al. 1990), and MS 0440+02 (Luppino et al. 1993).

4.2 Weak Lensing by Clusters — Arclets

In addition to the occasional giant arc, which is produced when a source happens to straddle a caustic, a lensing cluster also produces a large number of weakly distorted images of other background sources which are not located near caustics. These are the arclets. There is a population of distant blue galaxies in the universe whose spatial density reaches 50 – 100 galaxies per square arc minute at faint magnitudes (Tyson 1988). Each cluster therefore has on the order of 50 – 100 arclets per square arc minute exhibiting a coherent pattern of distortions. Arclets were first detected by Fort et al. (1988).

The separations between arclets, typically $\sim (5 - 10)''$, are much smaller than the scale over which the gravitational potential of a cluster as a whole changes appreciably. The weak and noisy signals from several individual arclets can therefore be averaged by statistical techniques to get an idea of the mass distribution of a cluster. This technique was first demonstrated by Tyson, Valdes, & Wenk (1990). Kochanek (1990) and Miralda-Escudé (1991a) studied how parameterized cluster lens models can be constrained with arclet data.

The first systematic and parameter-free procedure to convert the observed ellipticities of arclet images to a surface density map $\Sigma(\vec{\theta})$ of the lensing cluster was developed by Kaiser & Squires (1993). An ambiguity intrinsic to all such inversion methods which are based on shear information alone was identified by Seitz & Schneider (1995a). This ambiguity can be resolved by including information on the convergence of the cluster; methods for this were developed by Broadhurst, Taylor, & Peacock (1995) and Bartelmann & Narayan (1995a).

4.2.1 The Kaiser & Squires Algorithm

The technique of Kaiser & Squires (1993) is based on the fact that both convergence $\kappa(\vec{\theta})$ and shear $\gamma_{1,2}(\vec{\theta})$ are linear combinations of second derivatives of the effective lensing potential $\psi(\vec{\theta})$. There is thus a mathematical relation connecting the two. In the Kaiser & Squires method one first estimates $\gamma_{1,2}(\vec{\theta})$ by measuring the weak distortions of background galaxy images, and then uses the relation to infer $\kappa(\vec{\theta})$. The surface density of the lens is then obtained from $\Sigma(\vec{\theta}) = \Sigma_{\text{cr}}\kappa(\vec{\theta})$ (see eq. 49).

As shown in Sect. 3, κ and $\gamma_{1,2}$ are given by

$$\begin{aligned}\kappa(\vec{\theta}) &= \frac{1}{2} \left(\frac{\partial^2 \psi(\vec{\theta})}{\partial \theta_1^2} + \frac{\partial^2 \psi(\vec{\theta})}{\partial \theta_2^2} \right), \\ \gamma_1(\vec{\theta}) &= \frac{1}{2} \left(\frac{\partial^2 \psi(\vec{\theta})}{\partial \theta_1^2} - \frac{\partial^2 \psi(\vec{\theta})}{\partial \theta_2^2} \right), \\ \gamma_2(\vec{\theta}) &= \frac{\partial^2 \psi(\vec{\theta})}{\partial \theta_1 \partial \theta_2}.\end{aligned}\tag{79}$$

If we introduce Fourier transforms of κ , $\gamma_{1,2}$, and ψ (which we denote by hats on the symbols), we have

$$\hat{\kappa}(\vec{k}) = -\frac{1}{2} (k_1^2 + k_2^2) \hat{\psi}(\vec{k}),$$

$$\begin{aligned}
\hat{\gamma}_1(\vec{k}) &= -\frac{1}{2} (k_1^2 - k_2^2) \hat{\psi}(\vec{k}) , \\
\hat{\gamma}_2(\vec{k}) &= -k_1 k_2 \hat{\psi}(\vec{k}) ,
\end{aligned} \tag{80}$$

where \vec{k} is the two dimensional wave vector conjugate to $\vec{\theta}$. The relation between κ and $\gamma_{1,2}$ in Fourier space can then be written

$$\begin{aligned}
\begin{pmatrix} \hat{\gamma}_1 \\ \hat{\gamma}_2 \end{pmatrix} &= k^{-2} \begin{pmatrix} (k_1^2 - k_2^2) \\ 2k_1 k_2 \end{pmatrix} \hat{\kappa} , \\
\hat{\kappa} &= k^{-2} [(k_1^2 - k_2^2), (2k_1 k_2)] \begin{pmatrix} \hat{\gamma}_1 \\ \hat{\gamma}_2 \end{pmatrix} .
\end{aligned} \tag{81}$$

If the shear components $\gamma_{1,2}(\vec{\theta})$ have been measured, we can solve for $\hat{\kappa}(\vec{k})$ in Fourier space, and this can be back transformed to obtain $\kappa(\vec{\theta})$ and thereby $\Sigma(\vec{\theta})$. Equivalently, we can write the relationship as a convolution in $\vec{\theta}$ space,

$$\kappa(\vec{\theta}) = \frac{1}{\pi} \int d^2\theta' \operatorname{Re} \left[\mathcal{D}^*(\vec{\theta} - \vec{\theta}') \gamma(\vec{\theta}') \right] , \tag{82}$$

where \mathcal{D} is the complex convolution kernel,

$$\mathcal{D}(\vec{\theta}) = \frac{(\theta_2^2 - \theta_1^2) - 2i\theta_1\theta_2}{\theta^4} , \tag{83}$$

and $\gamma(\vec{\theta})$ is the complex shear,

$$\gamma(\vec{\theta}) = \gamma_1(\vec{\theta}) + i\gamma_2(\vec{\theta}) . \tag{84}$$

The asterisk denotes complex conjugation.

The key to the Kaiser & Squires method is that the shear field $\gamma(\vec{\theta})$ can be measured. (Elaborate techniques to do so were described by Bonnet & Mellier 1995 and Kaiser, Squires, & Broadhurst 1995.) If we define the ellipticity of an image as

$$\epsilon = \epsilon_1 + i\epsilon_2 = \frac{1-r}{1+r} e^{2i\phi} , \quad r \equiv \frac{b}{a} , \tag{85}$$

where ϕ is the position angle of the ellipse and a and b are its major and minor axes, respectively, we see from eq. (58) that the average ellipticity induced by lensing is

$$\langle \epsilon \rangle = \left\langle \frac{\gamma}{1-\kappa} \right\rangle , \tag{86}$$

where the angle brackets refer to averages over a finite area of the sky. In the limit of weak lensing, $\kappa \ll 1$ and $|\gamma| \ll 1$, and the mean ellipticity directly gives the shear,

$$\langle \gamma_1(\vec{\theta}) \rangle \approx \langle \epsilon_1(\vec{\theta}) \rangle , \quad \langle \gamma_2(\vec{\theta}) \rangle \approx \langle \epsilon_2(\vec{\theta}) \rangle . \tag{87}$$

The $\gamma_1(\vec{\theta})$, $\gamma_2(\vec{\theta})$ fields so obtained can be transformed using the integral (82) to obtain $\kappa(\vec{\theta})$ and thereby $\Sigma(\vec{\theta})$. The quantities $\langle \epsilon_1(\vec{\theta}) \rangle$ and $\langle \epsilon_2(\vec{\theta}) \rangle$ in (87) have to be obtained by averaging over sufficient numbers of weakly lensed sources to have a reasonable signal-to-noise ratio.

4.2.2 Practical Details and Subtleties

In practice, several difficulties complicate the application of the elegant inversion technique summarized by eq. (82). Atmospheric turbulence causes images taken by ground-based telescopes to

be blurred. As a result, elliptical images tend to be circularized so that ground-based telescopes measure a lower limit to the actual shear signal. This difficulty is not present for space-based observations.

The point-spread function of the telescope can be anisotropic and can vary across the observed field. An intrinsically circular image can therefore be imaged as an ellipse just because of astigmatism of the telescope. Subtle effects like slight tracking errors of the telescope or wind at the telescope site can also introduce a spurious shear signal.

In principle, all these effects can be corrected for. Given the seeing and the intrinsic brightness distribution of the image, the amount of circularization due to seeing can be estimated and taken into account. The shape of the point-spread function and its variation across the image plane of the telescope can also be calibrated. However, since the shear signal especially in the outskirts of a cluster is weak, the effects have to be determined with high precision, and this is a challenge.

The need to average over several background galaxy images introduces a resolution limit to the cluster reconstruction. Assuming 50 galaxies per square arc minute, the typical separation of two galaxies is $\sim 8''$. If the average is taken over ~ 10 galaxies, the spatial resolution is limited to $\sim 30''$.

We have seen in eq. (86) that the observed ellipticities strictly do not measure γ , but rather a combination of κ and γ ,

$$\langle \epsilon \rangle = \langle g \rangle \equiv \left\langle \frac{\gamma}{1 - \kappa} \right\rangle . \quad (88)$$

Inserting $\gamma = \langle \epsilon \rangle (1 - \kappa)$ into the reconstruction equation (82) yields an integral equation for κ which can be solved iteratively. This procedure, however, reveals a weakness of the method. Any reconstruction technique which is based on measurements of image ellipticities alone is insensitive to isotropic expansions of the images. The measured ellipticities are thus invariant against replacing the Jacobian matrix \mathcal{A} by some scalar multiple $\lambda \mathcal{A}$ of it. Putting

$$\mathcal{A}' = \lambda \mathcal{A} = \lambda \begin{pmatrix} 1 - \kappa - \gamma_1 & -\gamma_2 \\ -\gamma_2 & 1 - \kappa + \gamma_1 \end{pmatrix} , \quad (89)$$

we see that scaling \mathcal{A} with λ is equivalent to the following transformations of κ and γ ,

$$1 - \kappa' = \lambda (1 - \kappa) , \quad \gamma' = \lambda \gamma . \quad (90)$$

Manifestly, this transformation leaves g invariant. We thus have a one-parameter ambiguity in shear-based reconstruction techniques,

$$\kappa \rightarrow \lambda \kappa + (1 - \lambda) , \quad (91)$$

with λ an arbitrary scalar constant.

This invariance transformation was highlighted by Schneider & Seitz (1995) and was originally discovered by Falco, Gorenstein, & Shapiro (1985) in the context of galaxy lensing. If $\lambda \lesssim 1$, the transformation is equivalent to replacing κ by κ plus a sheet of constant surface mass density $1 - \lambda$. The transformation (91) is therefore referred to as the mass-sheet degeneracy.

Another weakness of the Kaiser & Squires method is that the reconstruction equation (82) requires a convolution to be performed over the entire $\vec{\theta}$ plane. Observational data however are available only over a finite field. Ignoring everything outside the field and restricting the range of integration to the actual field is equivalent to setting $\gamma = 0$ outside the field. For circularly symmetric mass distributions, this implies vanishing total mass within the field. The influence of the finiteness of the field can therefore be quite severe.

Finally, the reconstruction yields $\kappa(\vec{\theta})$, and in order to calculate the surface mass density $\Sigma(\vec{\theta})$ we must know the critical density Σ_{cr} , but since we do not know the redshifts of the sources there is a scaling uncertainty in this quantity. For a lens with given surface mass density, the distortion increases with increasing source redshift. If the sources are at much higher redshifts than the cluster, the influence of the source redshift becomes weak. Therefore, this uncertainty is less serious for low redshift clusters.

Nearly all the problems mentioned above have been addressed and solved. The solutions are discussed in the following subsections.

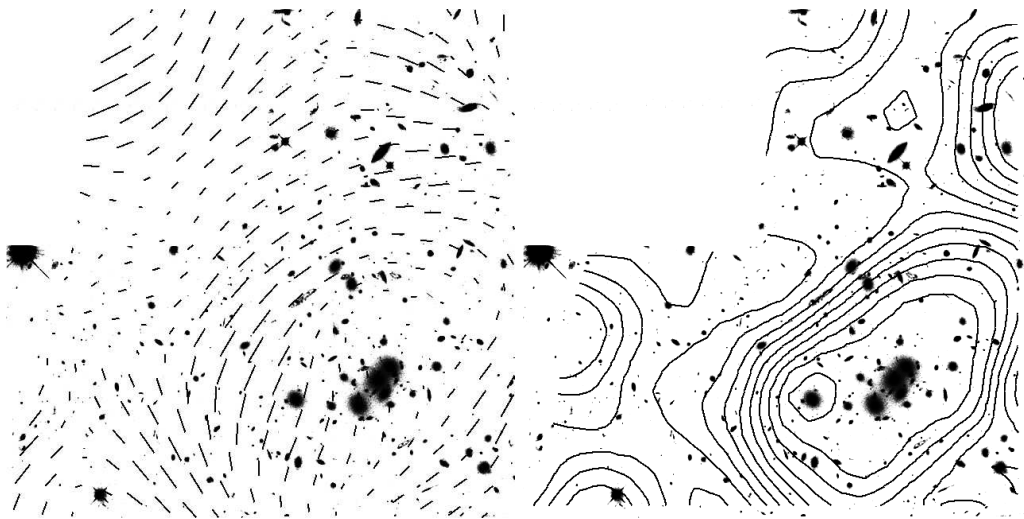


Figure 25: *HST* image of the cluster Cl 0024, overlaid on the left with the shear field obtained from an observation of arclets with the *Canada-France Hawaii Telescope* (Y. Mellier & B. Fort), and on the right with the reconstructed surface-mass density determined from the shear field (C. Seitz et al.). The reconstruction was done with a non-linear, finite-field algorithm.

4.2.3 Eliminating the Mass Sheet Degeneracy by Measuring the Convergence

By eq. (59),

$$\mu = \frac{1}{(1 - \kappa)^2 - \gamma^2}, \quad (92)$$

and so the magnification scales with λ as $\mu \propto \lambda^{-2}$. Therefore, the mass-sheet degeneracy can be broken by measuring the magnification μ of the images in addition to the shear (Broadhurst et al. 1995). Two methods have been proposed to measure μ . The first relies on comparing the galaxy counts in the cluster field with those in an unlensed “empty” field (Broadhurst et al. 1995). The observed counts of galaxies brighter than some limiting magnitude m are related to the intrinsic counts through

$$N'(m) = N_0(m) \mu^{2.5s-1}, \quad (93)$$

where s is the logarithmic slope of the intrinsic number count function,

$$s = \frac{d \log N(m)}{dm}. \quad (94)$$

In blue light, $s \sim 0.4$, and thus $N'(m) \sim N(m)$ independent of the magnification, but in red light $s \sim 0.15$, and the magnification leads to a dilution of galaxies behind clusters. The reduction of red galaxy counts behind the cluster A 1689 has been detected by Broadhurst (1995).

The other method is to compare the *sizes* of galaxies in the cluster field to those of similar galaxies in empty fields. Since lensing conserves surface brightness, it is most convenient to match galaxies with equal surface brightness while making this comparison (Bartelmann & Narayan 1995a). The magnification is then simply the ratio between the sizes of lensed and unlensed galaxies. Labeling galaxies by their surface brightness has the further advantage that the surface brightness is a steep function of galaxy redshift, which allows the user to probe the change of lens efficiency with source redshift (see below).

4.2.4 Determining Source Redshifts

For a given cluster, the strength of distortion and magnification due to lensing increases with increasing source redshift z_s . The mean redshift \bar{z}_s of sources as a function of apparent magnitude m can thus be inferred by studying the mean strength of the lensing signal vs. m (Kaiser 1995; Kneib et al. 1995).

The surface brightness S probably provides a better label for galaxies than the apparent magnitude because it depends steeply on redshift and is unchanged by lensing. Bartelmann & Narayan (1995a) have developed an algorithm, which they named the lens parallax method, to reconstruct the cluster mass distributions and to infer simultaneously \bar{z}_s as a function of the surface brightness. In simulations, data from ~ 10 cluster fields and an equal number of empty comparison fields were sufficient to determine the cluster masses to $\sim \pm 5\%$ and the galaxy redshifts to $\sim \pm 10\%$ accuracy. The inclusion of galaxy sizes in the iterative lens-parallax algorithm breaks the mass-sheet degeneracy, thereby removing the ambiguities in shear-based cluster reconstruction techniques arising from the transformation (91) and from the unknown redshift distribution of the sources.

4.2.5 Finite Field Methods

As emphasized previously, the inversion equation (82) requires a convolution to be performed over the entire real plane. The fact that data are always restricted to a finite field thus introduces a severe bias in the reconstruction. Modified reconstruction kernels have been suggested to overcome this limitation.

Consider the relation (Kaiser 1995)

$$\vec{\nabla}\kappa = \begin{pmatrix} \gamma_{1,1} + \gamma_{2,2} \\ \gamma_{2,1} - \gamma_{1,2} \end{pmatrix} \quad (95)$$

This shows that the convergence at any point $\vec{\theta}$ in the data field is related by a line integral to the convergence at another point $\vec{\theta}_0$,

$$\kappa(\vec{\theta}) = \kappa(\vec{\theta}_0) + \int_{\vec{\theta}_0}^{\vec{\theta}} d\vec{l} \cdot \vec{\nabla}\kappa[\vec{\theta}(\vec{l})]. \quad (96)$$

If the starting point $\vec{\theta}_0$ is far from the cluster center, $\kappa(\vec{\theta}_0)$ may be expected to be small and can be neglected. For each starting point $\vec{\theta}_0$, eq. (96) yields an estimate for $\kappa(\vec{\theta}) - \kappa(\vec{\theta}_0)$, and by averaging over all chosen $\vec{\theta}_0$ modified reconstruction kernels can be constructed (Schneider 1995; Kaiser et al. 1995; Bartelmann 1995c; Seitz & Schneider 1996). Various choices for the set of starting positions $\vec{\theta}_0$ have been suggested. For instance, one can divide the observed field into an inner region centered on the cluster and take as $\vec{\theta}_0$ all points in the rest of the field. Another possibility is to take $\vec{\theta}_0$ from the entire field. In both cases, the result is $\kappa(\vec{\theta}) - \bar{\kappa}$, where $\bar{\kappa}$ is the average convergence in the region from which the points $\vec{\theta}_0$ were chosen. The average $\bar{\kappa}$ is unknown, of course, and thus a reconstruction based on eq. (96) yields κ only up to a constant. Equation (96) therefore explicitly displays the mass sheet degeneracy since the final answer depends on the choice of the unknown $\kappa(\vec{\theta}_0)$.

A different approach (Bartelmann et al. 1996) employs the fact that κ and γ are linear combinations of second derivatives of the same effective lensing potential ψ . In this method one reconstructs ψ rather than κ . If both κ and γ can be measured through image distortions and magnifications (with different accuracies), then a straightforward finite-field Maximum-Likelihood can be developed to construct $\psi(\vec{\theta})$ on a finite grid such that it optimally reproduces the observed magnifications and distortions. It is easy in this approach to incorporate measurement accuracies, correlations in the data, selection effects etc. to achieve an optimal result.

4.2.6 Results from Weak Lensing

The cluster reconstruction technique of Kaiser & Squires and variants thereof have been applied to a number of clusters and several more are being analyzed. We summarize some results in Tab. 5,

Table 5: Mass-to-light ratios of several clusters derived from weak lensing.

Cluster	M/L	Remark	Reference
MS 1224	$800 h$	virial mass ~ 3 times smaller ($\sigma_v = 770 \text{ km s}^{-1}$) reconstruction out to $\sim 3'$	Fahlman et al. (1994)
A 1689	$(400 \pm 60) h$	mass smoother than light near center; mass steeper than isothermal from ($200 - 1000$) $h^{-1} \text{ kpc}$	Tyson & Fischer (1995) Kaiser (1995)
Cl 1455	$520 h$	dark matter more concen- trated than galaxies	Smail et al. (1995a)
Cl 0016	$740 h$	dark matter more concen- trated than galaxies	Smail et al. (1995a)
A 2218	$440 h$	gas mass fraction $< 4\% h^{-3/2}$	Squires et al. (1996a)
A 851	$200 h$	mass distribution agrees with galaxies and X-rays	Seitz et al. (1996)

focusing on the mass-to-light ratios of clusters and the degree of agreement between weak lensing and other independent studies of the same clusters.

Mass-to-light ratios inferred from weak lensing are generally quite high, $\sim 400 h$ in solar units. The recent detection of a significant shear signal in the cluster MS 1054–03 at redshift 0.83 (Luppino & Kaiser 1996) indicates that the source galaxies either are at very high redshifts, $z \gtrsim (2 - 3)$, or that the mass-to-light ratio in this cluster is exceptionally high; if the galaxy redshifts are $z \lesssim 1$, the mass-to-light ratio needs to be $\gtrsim 1600 h$.

The measurement of a coherent weak shear pattern out to a distance of almost 1.5 Mpc from the center of the cluster Cl 0024+1654 by Bonnet, Mellier, & Fort (1994) demonstrates a promising method of constraining cluster mass profiles. These observations show that the density decreases rapidly outward, though the data are compatible both with an isothermal profile and a steeper de Vaucouleurs profile. Tyson & Fischer (1995) find the mass profile in A 1689 to be steeper than isothermal. Squires et al. (1996b) derived the mass profile in A 2390 and showed that it is compatible with both an isothermal profile and steeper profiles. Quite generally, the weak-lensing results on clusters indicate that the smoothed light distribution follows the mass well. Moreover, mass estimates from weak lensing and from the X-ray emission interpreted on the basis of hydrostatic equilibrium are consistent with each other (Squires et al. 1996a,b).

4.3 Weak Lensing by Large-Scale Structure

4.3.1 Magnification and Shear in ‘Empty’ Fields

Lensing by even larger scale structures than galaxy clusters has been discussed in various contexts. Kristian & Sachs (1966) and Gunn (1967) discussed the possibility of looking for distortions in images of background galaxies due to weak lensing by large-scale foreground mass distributions. The idea has been revived and studied in greater detail by Babul & Lee (1991), Jaroszyński et al. (1990), Miralda-Escudé (1991b), Blandford et al. (1991), Bartelmann & Schneider (1991), Kaiser (1992), and Villumsen (1996). The effect is weak—magnification and shear are typically on the order of a few per cent—and a huge number of galaxies has to be imaged with great care before a coherent signal can be observed.

Despite the obvious practical difficulties, the rewards are potentially very interesting since the two-point correlation function of the image distortions gives direct information on the power

spectrum of density perturbations $P(k)$ in the universe. The correlation function of image shear, or *polarization* as it is sometimes referred to (Blandford et al. 1991), has been calculated for the standard CDM model and other popular models of the universe. Weak lensing probes mass concentrations on large scales where the density perturbations are still in the linear regime. Therefore, there are very few uncertainties in the theoretical interpretation of the phenomenon. The problems are expected to be entirely observational.

Using a deep image of a blank field, Mould et al. (1994) set a limit of $\bar{p} < 4$ per cent for the average polarization of galaxy images within a 4.8 arcminute field. This is consistent with most standard models of the universe. Fahlman et al. (1995) claimed a tighter bound, $\bar{p} < 0.9$ per cent in a 2.8 arcminute field. On the other hand, Villumsen (1995a), using the Mould et al. (1994) data, claimed a detection at a level of $\bar{p} = (2.4 \pm 1.2)$ per cent (95% confidence limit). There is clearly no consensus yet, but the field is still in its infancy.

Villumsen (1995b) has discussed how the two-point angular correlation function of faint galaxies is changed by weak lensing and how intrinsic clustering can be distinguished from clustering induced by lensing.

4.3.2 Large-Scale QSO-Galaxy Correlations

Fugmann (1990) noticed an excess of Lick galaxies in the vicinity of high-redshift, radio-loud QSOs and showed that the excess reaches out to $\sim 10'$ from the QSOs. If real, this excess is most likely caused by magnification bias due to gravitational lensing. Further, the scale of the lens must be very large. Galaxy-sized lenses have Einstein radii of a few arc seconds and are clearly irrelevant. The effect has to be produced by structure on scales much larger than galaxy clusters.

Following Fugmann's work, various other correlations of a similar nature have been found. Bartelmann & Schneider (1993b, 1994; see also Bartsch, Schneider, & Bartelmann 1996) discovered correlations between high-redshift, radio-loud, optically bright QSOs and optical and infrared galaxies, while Bartelmann, Schneider & Hasinger (1994) found correlations with diffuse X-ray emission in the 0.2 – 2.4 keV ROSAT band. Benítez & Martínez-González (1995) found an excess of red galaxies from the APM catalog around radio-loud QSOs with redshift $z \sim 1$ on scales $\lesssim 10'$. Seitz & Schneider (1995b) found correlations between the Bartelmann & Schneider (1993b) sample of QSOs and foreground Zwicky clusters. They followed in part an earlier study by Rodrigues-Williams & Hogan (1994), who found a highly significant correlation between optically-selected, high-redshift QSOs and Zwicky clusters. Later, Rodrigues-Williams & Hawkins (1995) detected similar correlations between QSOs selected for their optical variability and Zwicky clusters. Wu & Han (1995) searched for associations between distant radio-loud QSOs and foreground Abell clusters and found a marginally significant correlation with a subsample of QSOs.

All these results indicate that there are correlations between background QSOs and foreground “light” in the optical, infrared and soft X-ray wavebands. The angular scale of the correlations is compatible with that expected from lensing by large-scale structures. Bartelmann & Schneider (1993a, see also Bartelmann 1995a for an analytical treatment of the problem) showed that current models of large-scale structure formation can explain the observed large-scale QSO-galaxy associations, provided a double magnification bias (Borgeest, von Linde, & Refsdal 1991) is assumed. It is generally agreed that lensing by individual clusters of galaxies is insufficient to produce the observed effects if cluster velocity dispersions are of order 10^3 km s^{-1} (e.g. Rodrigues-Williams & Hogan 1994; Rodrigues-Williams & Hawkins 1995; Wu & Han 1995; Wu & Fang 1996). It appears, therefore, that lensing by large-scale structures has to be invoked to explain the observations. Bartelmann (1995a) has shown that constraints on the density perturbation spectrum and the bias factor of galaxy formation can be obtained from the angular cross-correlation function between QSOs and galaxies.

4.3.3 Outlook: Detecting Dark Matter Concentrations

If lensing is indeed responsible for the correlations discussed above, other signatures of lensing should be found. Fort et al. (1996) searched for shear due to weak lensing in the fields of five

luminous QSOs and found coherent signals in all five fields. In addition, they detected foreground galaxy groups for three of the sources. Earlier, Bonnet et al. (1993) had found evidence for a coherent shear pattern in the field of the lens candidate QSO 2345+007. The shear was later identified with a distant cluster (Mellier et al. 1994; Fischer et al. 1994).

In general, it appears that looking for weak coherent image distortions provides an excellent way of searching for otherwise invisible dark matter concentrations. A systematic technique for this purpose has been developed by Schneider (1996a). Weak lensing outside cluster fields may in the near future allow observers to obtain samples of mass concentrations which are selected purely on the basis of their lensing effect. Such a selection would be independent of the mass-to-light ratio, and would permit the identification and study of nonlinear structures in the universe with unusually large mass-to-light ratios. This would be complementary to the limits on compact masses discussed in Sect. 2.3.2.

Acknowledgements

The authors thank Rosanne DiStefano, Andreas Huss, Chris Kochanek, Tsafir Kolatt, Shude Mao, Peter Schneider and Uroš Seljak for helpful comments on the manuscript. This work was supported in part by NSF grant AST 9423209 and by the Sonderforschungsbereich SFB 375-95 of the Deutsche Forschungsgemeinschaft.

References

- [1] Alard, C. 1995, in: *Astrophysical Applications of Gravitational Lensing*, Proc. IAU Symp. 173, eds. C.S. Kochanek & J.N. Hewitt (Boston: Kluwer)
- [2] Alard, C., Mao, S., Guibert, J. 1995, *A&A*, 300, L17
- [3] Alcock, C., Akerlof, C.W., Allsman, R.A. et al. 1993, *Nat*, 365, 621
- [4] Alcock, C., Allsman, R., Axelrod, T. et al. 1995a, *Phys. Rev. Lett.*, 74, 2867
- [5] Alcock, C., Allsman, R.A., Alves, D. et al. 1995b, *ApJ*, 454, L125
- [6] Alcock, C., Allsman, R.A., Axelrod, T.S. et al. 1996a, *ApJ*, 461, 84
- [7] Alcock, C., Allsman, R.A., Axelrod, T.S. et al. 1996b, *ApJ*, submitted; preprint astro-ph/9512146
- [8] Ansari, R., Cavalier, F., Moniez, M. et al. 1996, *A&A*, in press; preprint astro-ph/9511073
- [9] Aubourg, E., Bareyre, P., Bréhin, P. et al. 1993, *Nat*, 365, 623
- [10] Aubourg, E., Bareyre, P., Bréhin, P. et al. 1995, *A&A*, 301, 1
- [11] Babul, A., Lee, M.H. 1991, *MNRAS*, 250, 407
- [12] Baillon, P., Bouquet, A., Giraud-Héraud, Y., Kaplan, J. 1993, *A&A*, 227, 1
- [13] Bar-Kana, R. 1996, *ApJ*, submitted; preprint astro-ph/9511056
- [14] Bartelmann, M. 1995a, *A&A*, 298, 661
- [15] Bartelmann, M. 1995b, *A&A*, 299, 11
- [16] Bartelmann, M. 1995c, *A&A*, 303, 643
- [17] Bartelmann, M. 1996, *A&A*, in press; preprint astro-ph/9602053
- [18] Bartelmann, M., Narayan, R. 1995a, *ApJ*, 451, 60

- [19] Bartelmann, M., Narayan, R. 1995b, in: *Dark Matter*, AIP Conf. Proc. 336, eds. S.S. Holt & C.L. Bennett (New York: AIP Press)
- [20] Bartelmann, M., Schneider, P. 1991, A&A, 248, 349
- [21] Bartelmann, M., Schneider, P. 1993a, A&A, 268, 1
- [22] Bartelmann, M., Schneider, P. 1993b, A&A, 271, 421
- [23] Bartelmann, M., Schneider, P. 1994, A&A, 284, 1
- [24] Bartelmann, M., Steinmetz, M. 1996, MNRAS, submitted; preprint astro-ph/9603101
- [25] Bartelmann, M., Weiss, A. 1994, A&A, 287, 1
- [26] Bartelmann, M., Schneider, P., Hasinger, G. 1994, A&A, 290, 399
- [27] Bartelmann, M., Steinmetz, M., Weiss, A. 1995, A&A, 297, 1
- [28] Bartelmann, M., Narayan, R., Seitz, S., Schneider, P. 1996, ApJ Letters, in press; preprint astro-ph/9601011
- [29] Bartsch, A., Schneider, P., Bartelmann, M. 1996, A&A, in press; preprint astro-ph/9601125
- [30] Benítez, N., Martínez-González, E. 1995, ApJ, 448, L89
- [31] Bennett, D.P., Alcock, C., Allsman, R. et al. 1995, in: *Dark Matter*, AIP Conf. Proc. 336, eds. S.S. Holt & C.L. Bennett (New York: AIP)
- [32] Bennett, D. 1996, in: *Microlensing*, Proc. 2nd International Workshop on Gravitational Microlensing Surveys, Orsay, France; ed. M. Moniez
- [33] Bergmann, A.G., Petrosian, V. 1993, ApJ, 413, 18
- [34] Bergmann, A.G., Petrosian, V., Lynds, R. 1990, ApJ, 350, 23
- [35] Blaes, O.M., Webster, R.L. 1992, ApJ, 391, L63
- [36] Blandford, R.D., Kochanek, C.S. 1987, ApJ, 321, 658
- [37] Blandford, R.D., Kochanek, C.S., Kovner, I., Narayan, R. 1989, Science, 245, 824
- [38] Blandford, R.D., Narayan, R. 1986, ApJ, 310, 568
- [39] Blandford, R.D., Narayan, R. 1992, ARA&A, 30, 311
- [40] Blandford, R.D., Saust, A.B., Brainerd, T.G., Villumsen, J.V. 1991, MNRAS, 251, 600
- [41] Bonnet, H., Mellier, Y. 1995, A&A, 303, 331
- [42] Bonnet, H., Mellier, Y., Fort, B. 1994, ApJ, 427, L83
- [43] Bonnet, H., Fort, B., Kneib, J.-P., Soucail, G., Mellier, Y. 1993, A&A, 289, L7
- [44] Borgeest, U., von Linde, J., Refsdal, S. 1991, A&A, 251, L35
- [45] Brainerd, T.G., Blandford, R.D., Smail, I. 1996, preprint astro-ph/9503073
- [46] Broadhurst, T. 1995, in: *Dark Matter*, AIP Conf. Proc. 336, eds. S.S. Holt & C.L. Bennett (New York: AIP)
- [47] Broadhurst, T., Taylor, A., Peacock, J. 1995, ApJ, 438, 49
- [48] Burke, W.L. 1981, ApJ, 244, L1

- [49] Canizares, C.R. 1982, ApJ, 263, 508
- [50] Carlberg, R.G. 1994, ApJ, 433, 468
- [51] Carlberg, R.G., Yee, H.K.C., Ellingson, E. 1994, ApJ, 437, 63
- [52] Carr, B. 1994, ARA&A, 32, 531
- [53] Cen, R.Y., Gott III, J.R., Ostriker, J.P., Turner, E.L. 1994, ApJ, 423, 1
- [54] Chang, K., Refsdal, S. 1979, Nat, 282, 561
- [55] Chwolson, O. 1924, Astron. Nachr., 221, 329
- [56] Colley, W.N. 1995, AJ, 109, 440
- [57] Corbett, E.A., Browne, I.W.A., Wilkinson, P.N., Patnaik, A.R. 1996, in: *Astrophysical Applications of Gravitational Lensing*, Proc. IAU Symp. 173, eds. C.S. Kochanek & J.N. Hewitt (Boston: Kluwer)
- [58] Corrigan, R.T., Irwin, M.J., Arnaud, J., Fahlman, G.G., Fletcher, J.M. et al. 1991, AJ, 102, 34
- [59] Crotts, A.P. S. 1992, ApJ, 399, L43
- [60] Daines, S., Jones, C., Forman, W., Tyson, A. 1996, preprint
- [61] Dalcanton, J.J., Canizares, C.R., Granados, A., Steidel, C.C., Stocke, J.T. 1994, ApJ, 424, 550
- [62] Di Stefano, R., Esin, A.A. 1995, ApJ, 448, L1
- [63] Di Stefano, R., Mao, S. 1996, ApJ, 457, 93
- [64] Durret, F., Gerbal, D., Lachièze-Rey, M., Lima-Neto, G., Sadat, R. 1994, A&A, 287, 733
- [65] Dyson, F.W., Eddington, A.S., & Davidson, C.R. 1920, Mem. R. Astron. Soc., 62, 291
- [66] Eddington, A.S. 1920, Space, Time and Gravitation (Cambridge: University Press)
- [67] Einstein, A. 1911, Annalen der Physik, 35, 898
- [68] Einstein, A. 1915, Sitzungsber. Preuß. Akad. Wissensch., erster Halbband, p. 831
- [69] Einstein, A. 1936, Sci, 84, 506
- [70] Erdl, H., Schneider, P. 1992, A&A, 268, 453
- [71] Fahlman, G., Kaiser, N., Squires, G., Woods, D. 1994, ApJ, 437, 56
- [72] Falco, E.E., Gorenstein, M.V., Shapiro, I.I. 1985, ApJ, 289, L1
- [73] Falco, E.E., Gorenstein, M.V., Shapiro, I.I. 1991, ApJ, 372, 364
- [74] Fischer, P., Tyson, J.A., Bernstein, G.M., Guhathakurta, P. 1994, ApJ, 431, L71
- [75] Flores, R., Primack, J. 1996, ApJ, 457, L5
- [76] Fort, B., Mellier, Y. 1994, A&AR, 5, 239
- [77] Fort, B., Prieur, J.L., Mathez, G., Mellier, Y., Soucail, G. 1988, A&A, 200, L17
- [78] Fort, B., Le Fèvre, O., Hammer, F., Cailloux, M. 1992, ApJ, 399, L125

- [79] Fort, B., Mellier, Y., Dantel-Fort, M., Bonnet, H., Kneib, J.-P. 1995, A&A, submitted; preprint astro-ph/9507076
- [80] Fugmann, W. 1990, A&A, 240, 11
- [81] Fukugita, M., Turner, E.L. 1991, MNRAS, 253, 99
- [82] Fukugita, M., Futamase, T., Kasai, M., Turner, E.L. 1992, ApJ, 393, 3
- [83] Garrett, M.A., Calder, R.J., Porcas, R.W., King, L.J., Walsh, D., Wilkinson, P.N. 1994, MNRAS, 270, 457
- [84] Gerbal, D., Durret, F., Lima-Neto, G., Lachière-Rey, M. 1992, A&A, 253, 77
- [85] Gorenstein, M.V., Cohen, N.L., Shapiro, I.I., Rogers, A.E.E., Bonometti, R.J., Falco, E.E., Bartel, N., Marcaide, J.M. 1988, ApJ, 334, 42
- [86] Gott, J.R. 1981, ApJ, 243, 140
- [87] Gould, A. 1992a, ApJ, 386, L5
- [88] Gould, A. 1992b, ApJ, 392, 442
- [89] Gould, A. 1994a, ApJ, 421, L71
- [90] Gould, A. 1994b, ApJ, 421, L75
- [91] Gould, A., Loeb, A. 1992, ApJ, 396, 104
- [92] Griest, K. 1991, ApJ, 366, 412
- [93] Griest, K., Hu, W. 1992, ApJ, 397, 362
- [94] Griest, K., Alcock, C., Axelrod, T.S. 1991, ApJ, 372, L79
- [95] Grogin, N., & Narayan, R. 1996, ApJ, in press; preprint astro-ph/9512156
- [96] Grossman, S.A., Narayan, R. 1988, ApJ, 324, L37
- [97] Grossman, S.A., Narayan, R. 1989, ApJ, 344, 637
- [98] Grossman, S.A., Saha, P. 1994, ApJ, 431, 74
- [99] Gunn, J.E. 1967, ApJ, 150, 737
- [100] Hammer, F. 1991, ApJ, 383, 66
- [101] Hammer, F., Rigaut, F. 1989, A&A, 226, 45
- [102] Henstock, D.R., Browne, I.W.A., Wilkinson, P.N., Taylor, G.B., Vermeulen, R.C., Pearson, T.J., Readhead, R.C.S. 1995, ApJS, 100, 1
- [103] Haarsma, D.B., Hewitt, J.N., Burke, B.F., Lehár, J. 1996, in: *Astrophysical Applications of Gravitational Lensing*, IAU Symp. 173, eds. C.S. Kochanek & J.N. Hewitt (Boston: Kluwer)
- [104] Hewitt, J.N., Turner, E.L., Lawrence, C.R., Schneider, D.P., Gunn, J.E. et al. 1987, ApJ, 321, 706
- [105] Huchra, J., Gorenstein, M., Kent, S., Shapiro, I., Smith, G. et al. 1985, AJ, 90, 691
- [106] Irwin, M.J., Webster, R.L., Hewett, P.C., Corrigan, R.T., Jedrzejewski, R.I. 1989, AJ, 98, 1989
- [107] Jaroszyński, M., Park, C., Paczyński, B., Gott, J.R. 1990, ApJ, 365, 22

- [108] Kaiser, N. 1992, ApJ, 388, 272
- [109] Kaiser, N. 1995, ApJ, 439, L1
- [110] Kaiser, N., Squires, G. 1993, ApJ, 404, 441
- [111] Kaiser, N., Squires, G., Broadhurst, T. 1995, ApJ, 449, 460
- [112] Kaiser, N., Squires, G., Fahlman, G., Woods, D., Broadhurst, T. 1995, in: Proc. 35th Herstmonceux Conf., ed. S. Maddox (Singapore: World Scientific)
- [113] Kamionkowski, M. 1995, ApJ, 442, L9
- [114] Kassiola, A., Kovner, I. 1993, ApJ, 417, 450
- [115] Kassiola, A., Kovner, I., Blandford, R.D. 1991, ApJ, 381, 6
- [116] Kassiola, A., Kovner, I., Blandford, R.D. 1992, ApJ, 396, 10
- [117] Keeton II, C.R., Kochanek, C.S. 1996, in: *Astrophysical Applications of Gravitational Lensing*, IAU Symp. 173, eds. C.S. Kochanek & J.N. Hewitt (Boston: Kluwer)
- [118] Kiraga, M., Paczyński, B. 1994, ApJ, 430, L101
- [119] Kneib, J.-P., Ellis, R.S., Smail, I., Couch, W.T., Sharples, R.M. 1995, ApJ, submitted; preprint astro-ph/9511015
- [120] Kneib, J.-P., Mellier, Y., Fort, B., Mathez, G. 1993, A&A, 273, 367
- [121] Kochanek, C.S. 1990, MNRAS, 247, 135
- [122] Kochanek, C.S. 1991, ApJ, 373, 354
- [123] Kochanek, C.S. 1992, ApJ, 384, 1
- [124] Kochanek, C.S. 1993a, ApJ, 417, 438
- [125] Kochanek, C.S. 1993b, ApJ, 419, 12
- [126] Kochanek, C.S. 1995a, ApJ, 445, 559
- [127] Kochanek, C.S. 1995b, ApJ, 453, 545
- [128] Kochanek, C.S. 1996a, ApJ, in press; preprint astro-ph/9510077
- [129] Kochanek, C.S. 1996b, ApJ, submitted; preprint CfA #4283
- [130] Kochanek, C.S., Narayan, R. 1992, ApJ, 401, 461
- [131] Kochanek, C.S., Blandford, R.D., Lawrence, C.R., Narayan, R. 1989, MNRAS, 238, 43
- [132] Kovner, I. 1987, ApJ, 312, 22
- [133] Kovner, I. 1989, ApJ, 337, 621
- [134] Kristian, J., Sachs, R.K. 1966, ApJ, 143, 379
- [135] Le Fèvre, O., Hammer, F., Angonin-Willaime, M.-C., Gioia, I.M., Luppino, G.A. 1994, ApJ, 422, L5
- [136] Lehár, J., Hewitt, J.N., Roberts, D.H., Burke, B.F. 1992, ApJ, 384, 453
- [137] Loeb, A., Mao, S. 1994, ApJ, 435, L109

- [138] Luppino, G.A., Gioia, I.M., Annis, J., Le Fèvre, O., Hammer, F. 1993, ApJ, 416, 444
- [139] Luppino, G.A., Kaiser, N. 1996, ApJ, submitted; preprint astro-ph/9601194
- [140] Lynds, R., Petrosian, V. 1986, BAAS, 18, 1014
- [141] Mao, S., Paczyński, B. 1991, ApJ, 374, L37
- [142] Mao, S., Kochanek, C.S. 1994, MNRAS, 268, 569
- [143] Maoz, D., Rix, H.-W. 1993, ApJ, 416, 425
- [144] Mathez, G., Fort, B., Mellier, Y., Picat, J.-P., Soucail, G. 1992, A&A, 256, 343
- [145] Mellier, Y., Fort, B., Kneib, J.-P. 1993, ApJ, 407, 33
- [146] Mellier, Y., Dantel-Fort, M., Fort, B., Bonnet, H. 1994, A&A, 289, L15
- [147] Miralda-Escudé, J. 1991a, ApJ, 370, 1
- [148] Miralda-Escudé, J. 1991b, ApJ, 380, 1
- [149] Miralda-Escudé, J. 1992, ApJ, 390, L65
- [150] Miralda-Escudé, J. 1993, ApJ, 403, 497
- [151] Miralda-Escudé, J. 1995, ApJ, 438, 514
- [152] Miralda-Escudé, J., Babul, A. 1995, ApJ, 449, 18
- [153] Mould, J., Blandford, R.D., Villumsen, J.V., Brainerd, T.G., Smail, I., Small, T., Kells, W. 1994, MNRAS, 271, 31
- [154] Narayan, R. 1991, ApJ, 378, L5
- [155] Narayan, R., Grossman, S. 1989, in: *Gravitational Lenses*, eds. J.M. Moran, J.N. Hewitt, K.Y. Lo (Berlin: Springer-Verlag)
- [156] Narayan, R., White, S.D.M. 1988, MNRAS, 231, 97P
- [157] Narayan, R., Wallington, S. 1993, in: *Gravitational Lenses in the Universe*, Proc. 31st Liège Astroph. Coll., eds. J. Surdej et al.
- [158] Narayan, R., Blandford, R.D., Nityananda, R. 1984, Nat, 310, 112
- [159] Navarro, J.F., Frenk, C.S., White, S.D.M. 1996, MNRAS, in press; preprint astro-ph/9508025
- [160] Nemiroff, R.J., Wickramasinghe, W.A.D.T. 1994, ApJ, 424, L21
- [161] Nemiroff, R.J., Norris, J.P., Wickramasinghe, W.A.D.T., Horack, J.M., Kouveliotou, C. et al. 1993, ApJ, 414, 36
- [162] Nemiroff, R.J., Wickramasinghe, W.A.D.T., Norris, J.P., Kouveliotou, C., Fishman, G.J. et al. 1994, ApJ, 432, 478
- [163] Nityananda, R., Samuel, J. 1992, Phys. Rev. D, 45, 3862
- [164] Østensen, R., Refsdal, S., Stabell, R., Teuber, J., Emanuelsen, P.I. et al.: 1996, A&A, 309, 59
- [165] Paczyński, B. 1986a, ApJ, 301, 503
- [166] Paczyński, B. 1986b, ApJ, 304, 1

- [167] Paczyński, B. 1987, *Nat*, 325, 572
- [168] Paczyński, B. 1991, *ApJ*, 371, L63
- [169] Paczyński, B. 1996, *ARA&A*, in press; preprint astro-ph/9604011
- [170] Paczyński, B., Stanek, K.Z., Udalski, A., Szymański, M., Kahunz, J., Kubiak, M., Mateo, M., Krzemiński, W. 1994, *ApJ*, 435, L113
- [171] Pelló-Descayre, R., Soucail, G., Sanahuja, B., Mathez, G., Ojero, E. 1988, *A&A*, 190, L11
- [172] Pelló, R., Le Borgne, J.F., Soucail, G., Mellier, Y., Sanahuja, B. 1991, *ApJ*, 366, 405
- [173] Pelt, J., Hoff, W., Kayser, R., Refsdal, S., Schramm, T. 1994, *A&A*, 286, 775
- [174] Pelt, J., Kayser, R., Refsdal, S., Schramm, T. 1996, *A&A*, 305, 97
- [175] Pierre, M., Le Borgne, J.F., Soucail, G., Kneib, J.P. 1996, *A&A*, submitted; preprint astro-ph/9510128
- [176] Pratt, M. 1996, in: *Microlensing*, Proc. 2nd International Workshop on Gravitational Microlensing Surveys, Orsay, France; ed. M. Moniez
- [177] Press, W.H., Gunn, J.E. 1973, *ApJ*, 185, 397
- [178] Press, W.H., Rybicki, G.B., Hewitt, J.N. 1992a, *ApJ*, 385, 404
- [179] Press, W.H., Rybicki, G.B., Hewitt, J.N. 1992b, *ApJ*, 385, 416
- [180] Rauch, K.P., Blandford, R.D. 1991, *ApJ*, 381, L39
- [181] Refsdal, S. 1964, *MNRAS*, 128, 307
- [182] Refsdal, S. 1966a, *MNRAS*, 132, 101
- [183] Refsdal, S. 1966b, *MNRAS*, 134, 315
- [184] Refsdal, S., Surdej, J. 1994, *Rep. Progr. Phys.*, 57, 117
- [185] Rix, H.-W., Maoz, D., Turner, E.L., Fukugita, M. 1994, *ApJ*, 435, 49
- [186] Rodrigues-Williams, L.L., Hogan, C.J. 1994, *AJ*, 107, 451
- [187] Rodrigues-Williams, L.L., Hawkins, M.R.S. 1995, in: *Dark Matter*, AIP Conf. Proc. 336, eds. S.S. Holt & C.L. Bennett (New York: AIP)
- [188] Roulet, E., Mollerach, S. 1996, *Phys. Reports*, in press; preprint astro-ph/9603119
- [189] Sackett, P.D. 1996, in: *Microlensing*, Proc. 2nd International Workshop on Gravitational Microlensing Surveys, Orsay, France; ed. M. Moniez
- [190] Sahu, K.C. 1994, *Nat*, 370, 275
- [191] Sahu, K.C. 1996, in: *Microlensing*, Proc. 2nd International Workshop on Gravitational Microlensing Surveys, Orsay, France; ed. M. Moniez
- [192] Schild, R.E., Smith, R.C. 1991, *AJ*, 101, 813
- [193] Schild, R.E., Thomson, D.J. 1993, in: *Gravitational Lenses in the Universe*, Proc. 31st Liège Int. Astroph. Coll., eds. J. Surdej et al.
- [194] Schmidt, M. 1963, *Nat*, 197, 1040
- [195] Schneider, P. 1985, *A&A*, 143, 413

- [196] Schneider, P. 1993, A&A, 279, 1
- [197] Schneider, P. 1995, A&A, 302, 639
- [198] Schneider, P. 1996a, MNRAS, submitted; preprint astro-ph/9601039
- [199] Schneider, P. 1996b, in: *Cosmological Applications of Gravitational Lensing*, Lecture Notes in Physics, eds. E. Martínez-González & J.L. Sanz, in press (Berlin: Springer Verlag)
- [200] Schneider, P., Seitz, C. 1995, A&A, 294, 411
- [201] Schneider, P., Weiss, A. 1987, A&A, 171, 49
- [202] Schneider, P., Ehlers, J., Falco, E.E. 1992, *Gravitational Lenses* (Berlin: Springer Verlag)
- [203] Seitz, C., Schneider, P. 1995a, A&A, 297, 287
- [204] Seitz, C., Wambsganss, J., Schneider, P. 1994, A&A, 288, 19
- [205] Seitz, C., Kneib, J.-P., Schneider, P., Seitz, S. 1996, A&A, submitted; preprint astro-ph/9601078
- [206] Seitz, S., Schneider, P. 1995b, A&A, 302, 9
- [207] Seitz, S., Schneider, P. 1996, A&A, 305, 383
- [208] Seljak, U. 1994, ApJ, 436, 509
- [209] Shapiro, I.I. 1964, Phys. Rev. Lett., 13, 789
- [210] Smail, I., Dickinson, M. 1995, ApJ, 455, L99
- [211] Smail, I., Ellis, R.S., Fitchett, M.J., Edge, A.C. 1995a, MNRAS, 273, 277
- [212] Smail, I., Dressler, A., Kneib, J.-P., Ellis, R.S., Couch, W.J., Sharples, R.M., Oemler Jr., A. 1995b, preprint astro-ph/9503063
- [213] Smail, I., Ellis, R.S., Fitchett, M.J., Norgaard-Nielsen, H.U., Hansen, L., Jorgensen, H.J. 1991, MNRAS, 252, 19
- [214] Soldner, J. 1804, Berliner Astron. Jahrb. 1804, p. 161
- [215] Soucaill, G., Fort, B., Mellier, Y., Picat, J.P. 1987a, A&A, 172, L14
- [216] Soucaill, G., Mellier, Y., Fort, B., Hammer, F., Mathez, G. 1987b, A&A, 184, L7
- [217] Squires, G., Kaiser, N., Babul, A., Fahlman, G., Woods, D., Neumann, D., Böhringer, H. 1996a, ApJ, 461, 572
- [218] Squires, G., Kaiser, N., Fahlman, G., Babul, A., Woods, D., 1996b, ApJ, submitted; preprint astro-ph/9602105
- [219] Stanek, K.Z., Paczyński, B., Goodman, J. 1993, ApJ, 413, L7
- [220] Subramanian, K., Cowling, S.A. 1986, MNRAS, 219, 333
- [221] Surdej, J., Claeskens, J.-F., Crampton, D., Filippenko, A.V., Hutsemékers, D. et al. 1993, AJ, 105, 2064
- [222] Turner, E.L. 1980, ApJ, 242, L135
- [223] Turner, E.L. 1990, ApJ, 365, L43
- [224] Turner, E.L., Ostriker, J.P., Gott, J.R. 1984, ApJ, 284, 1

- [225] Tyson, J.A. 1988, *AJ*, 96, 1
- [226] Tyson, J.A. 1990, *Gravitational Lensing*, Proc. Workshop Toulouse 1989 (Berlin: Springer)
- [227] Tyson, J.A. 1995, in: *Dark Matter*, AIP Conf. Proc 336, eds. S.S. Holt & C.L. Bennett (New York: AIP)
- [228] Tyson, J.A., Valdes, F., Wenk, R.A. 1990, *ApJ*, 349, L1
- [229] Tyson, J.A., Fischer, P. 1995, *ApJ*, 446, L55
- [230] Udalski, A., Szymański, M., Kałuzny, J., Kubiak, M., Mateo, M. 1992, *Acta Astron.*, 42, 253
- [231] Udalski, A., Szymański, M., Kałuzny, J., Kubiak, M., Krzemiński, W. et al. 1993, *Acta Astron.* 43, 289
- [232] Udalski, A., Szymański, M., Mao, S., Di Stefano, R., Kałuzny, J., Kubiak, M., Mateo, M., Krzemiński, W. 1994, *ApJ*, 436, L103
- [233] Vanderriest, C., Schneider, J., Herpe, G., Chèvreton, M., Moles, M., Wlérick, G. 1989, *A&A*, 215, 1
- [234] Villumsen, J.V. 1995a, *MNRAS*, submitted; preprint astro-ph/9507007
- [235] Villumsen, J.V. 1995b, *MNRAS*, submitted; preprint astro-ph/9512001
- [236] Villumsen, J.V. 1996, *MNRAS*, in press; preprint astro-ph/9503011
- [237] Walsh, D., Carswell, R.F., & Weymann, R.J. 1979, *Nat*, 279, 381
- [238] Wallington, S., Narayan, R. 1993, *ApJ*, 403, 517
- [239] Wallington, S., Kochanek, C.S., Koo, D.C. 1995, *ApJ*, 441, 58
- [240] Wallington, S., Kochanek, C.S., Narayan, R. 1996, *ApJ*, in press; preprint astro-ph/9511137
- [241] Wallington, S., Narayan, R., Kochanek, C.S. 1994, *ApJ*, 426, 60
- [242] Wambsganss, J. 1990, Ph.D. Thesis, MPA report #550
- [243] Wambsganss, J., Paczyński, B., Schneider, P. 1990, *ApJ*, 358, L33
- [244] Wambsganss, J., Cen, R.Y., Ostriker, J.P., Turner, E.L. 1995, *Sci*, 268, 274
- [245] Webster, R.L., Ferguson, A.M.N., Corrigan, R.T., Irwin, M.J. 1991, *AJ*, 102, 1939
- [246] Witt, H.J. 1993, *ApJ*, 403, 530
- [247] Witt, H.J. 1995, *ApJ*, 449, 42
- [248] Witt, H.J., Mao, S. 1994, *ApJ*, 430, 505
- [249] Wu, X.-P. 1996, *Fund. Cosmic Phys.*, in press; preprint astro-ph/9512110
- [250] Wu, X.-P., Hammer, F. 1993, *MNRAS*, 262, 187
- [251] Wu, X.-P., Han, J. 1995, *MNRAS*, 272, 705
- [252] Wu, X.-P., Fang, L.-Z. 1996, *ApJ*, 461, L5
- [253] Zhao, H.S., Spergel, D.N., Rich, R.M., *ApJ*, 440, L13
- [254] Zwicky, F. 1937a, *Phys. Rev. Lett.*, 51, 290
- [255] Zwicky, F. 1937b, *Phys. Rev. Lett.*, 51, 679

This figure "fig401.jpg" is available in "jpg" format from:

<http://arxiv.org/ps/astro-ph/9606001v1>